Novel correlative microscopy approach for nano-bio interface studies of nanoparticle-induced lung epithelial cell damage

Rok Podlipec[1,2*], Luka Pirker[1,3], Ana Krišelj[1], Gregor Hlawacek[2], Alessandra Gianoncelli[4], Primož Pelicon[1]

[1] Jožef Stefan Institute, Jamova cesta 39, 1000 Ljubljana, Slovenia

[2] Helmholtz-Zentrum Dresden-Rossendorf e.V., Institute for Ion Beam Physics and Materials Research, Bautzner Landstrasse 400, 01328 Dresden, Germany

[3] J. Heyrovský Institute of Physical Chemistry, v.v.i., Department of Electrochemical Materials, Dolejškova 3, 182 23 Prague 8, Czech Republic

[4] Elettra, Sincrotrone Trieste, Strada Statale 14 - km 163,5 in AREA Science Park, Trieste, Italy

* E-mail: rok.podlipec@ijs.si

Abstract

Correlated light and electron microscopy (CLEM) has become essential in life sciences due to advancements in imaging resolution, sensitivity, and sample preservation. In nanotoxicology—specifically, studying the health effects of particulate matter exposure—CLEM can enable molecular-level structural as well as functional analysis of nanoparticle interactions with lung tissue, key for the understanding of modes of action. In our study, we for the first time implement an integrated high-resolution fluorescence lifetime imaging microscopy (FLIM) and hyperspectral fluorescence imaging (fHSI), scanning electron microscopy (SEM), ultra-high resolution helium ion microscopy (HIM) and synchrotron micro X-ray fluorescence (SR μXRF), to characterize the nano-bio interface and to better elucidate the modes of action of lung epithelial cells response to known inflammatory titanium dioxide nanotubes (TiO_2 NTs). Morpho-functional assessment uncovered several mechanisms associated with the extensive DNA, essential minerals and iron accumulation, cellular surface immobilization, and the localized formation of fibrous structures, all confirming immunomodulatory responses. These findings advance our understanding of the early cellular processes leading to inflammation development after lung epithelium exposure to these, high-aspect-ratio nanoparticles. The novel experimental approach, exploiting light, ion and

electron sources, provides a robust framework for future research into nanoparticle toxicity and its impact on human health.

Keywords: nano-bio interface, TiO_2 nanotubes, lung epithelium inflammation, correlated light and electron microscopy, synchrotron micro X-Ray fluorescence, helium ion microscopy

Introduction

Among the novel microscopy approaches, correlated light and electron microscopy (CLEM) has attracted considerable interest in the life sciences community, particularly following recent developments in the spatial resolution and sensitivity capabilities of individual techniques.[1,2] Advanced live cell imaging, with its targeted labelling of individual cellular components, can provide molecular specificity and the observation of dynamic changes.[3,4] In addition, the advanced imaging of fixed cells, when performed in high vacuum, can provide ultrastructural information with nanometer spatial resolution [5] and chemical information with sub-micron resolution.[6,7] When successfully combined on the same region of interest (ROI), a correlative microscopy approach offers several significant advantages. It provides comprehensive functional and structural insights at multiple scales, as well as increased accuracy through cross-validation of data and improved contextual understanding through the analysis of dynamic and static processes on live and fixed cells, respectively.

One of the highly relevant scientific areas that can be addressed by correlative microscopy is the field of nanotoxicology, which studies the environmental and, in particular, health effects of the ubiquitous particulate matter in the polluted air.[8] In particular, ambient ultrafine particles (UFPs) and engineered nanomaterials (NMs) less than 100 nm in size can penetrate deep into the lungs and induce a variety of chronic diseases, including inflammation, fibrosis and cancer. [9–11] For safety assessment and prediction of nanoparticle-induced adverse outcomes, understanding of the mode of action at the molecular level, starting from the moment the particles interact with the lung tissue, is critical. To this end, several innovative correlative microscopy approaches have been introduced in recent years to elucidate the interaction at the nano-bio interface and the subsequent impact of nanomaterials and/or elements on biological matter.[12–36] A commonly used approach is CLEM[12] which mostly combines highly specific and targeted fluorescence microscopy (FM) with transmission electron microscopy (TEM).[13–15] More recently, super-resolution fluorescence imaging combined with TEM and scanning electron microscopy (SEM) has been implemented to address the complex biological questions at the nanoscale.[16]

While CLEM remains a prominent approach, recent years have seen the development of several complementary techniques. These correlate FM with X-ray tomography[17], dark-field microscopy (DFM)[18], atomic force microscopy (AFM)[19,20], and ion-induced luminescence.[21] Additionally, to enhance and support CLEM, a few ion-based methods have also been introduced.[22,23] For more detailed and quantitative analysis of the specific molecules and elements present in biological tissues, correlative microscopy approaches often include secondary ion mass spectrometry (SIMS) combined with electron microscopy[24–26] and novel high-resolution helium ion microscopy (HIM).[27–29] In addition to SIMS, proton-induced X-ray emission (PIXE) and X-ray fluorescence (XRF) analytical techniques are also used to quantify chemical elements in biological samples, and are combined with FM[30] and EM[31,32], respectively. Other correlative approaches include the combination of XRF with AFM[33] or XRF with ion beam techniques[34–36] for elemental quantification and complementary information.

Despite the continuous development of new correlative microscopy approaches in nanomaterial toxicity research, the full potential of multimodalities and their combinations has not yet been fully exploited, with many opportunities and challenges.[37] In this study, we present a novel correlative microscopy pipeline that can investigate the modes of action and toxic effects of UFPs and NMs, both of which pose the greatest risk to the lungs, as they can penetrate deep into the alveolar region and potentially further into the bloodstream.[38] We are particularly focused on the worldwide and one of the most widely used industrial NMs, titanium dioxide (TiO_2), which in the form of high surface area nanotubes (NTs) induces lung inflammatory[39,40] and is likely to be carcinogenic for humans.[41] We demonstrate the utility of an innovative multimodal and multiscale experimental workflow that integrates several complementary imaging and spectroscopy techniques on live and fixed cells in a high vacuum (Figure 1). In order to preserve the nanoscale morphology and properties of the investigated nano-bio interfaces on the surfaces, we use a rapid cryofixation technique without chemical cross-linking, which could otherwise compromise sample size, shape or cell membranes at the investigated spatial scale.[42–46] We must acknowledge that the development of sample preparation and preservation for high-vacuum, high-resolution correlative microscopy is one of the major challenges in the field and can play a key role in influencing the physicochemical properties of samples and the subsequent interpretation of results.[7,33,34,37,47]

The present study aims to cover a wide range of detectable spatial scales (down to the nanometer level) and to gain insight into both functional and structural properties of the samples under investigation. In order to obtain comprehensive knowledge, data gathered from multimodal

96 fluorescence microspectroscopy performed on living cells were integrated with data obtained from
97 high resolution and high elemental sensitivity X-ray, ion and electron-based techniques performed
98 in high vacuum. These approaches provided new insights into the physicochemical properties of
99 cell-excreted and cell-deposited TiO_2-biological matter (TiO_2-bio) composites aggregated and
100 immobilized on the surface of the lung epithelium. In addition, we gained deeper morpho-
101 functional insights into the inflammatory and anti-inflammatory mechanisms triggered by the
102 binding and transport of DNA and other molecules to TiO_2 NTs. We also uncovered the possible
103 mechanism of an initiation of an acute cellular response via the formation of a fibrous network
104 over the nanoparticles. These findings contribute to a deeper understanding of the current
105 knowledge in the field of UFPs and NMs-induced toxicity on the lung epithelium.

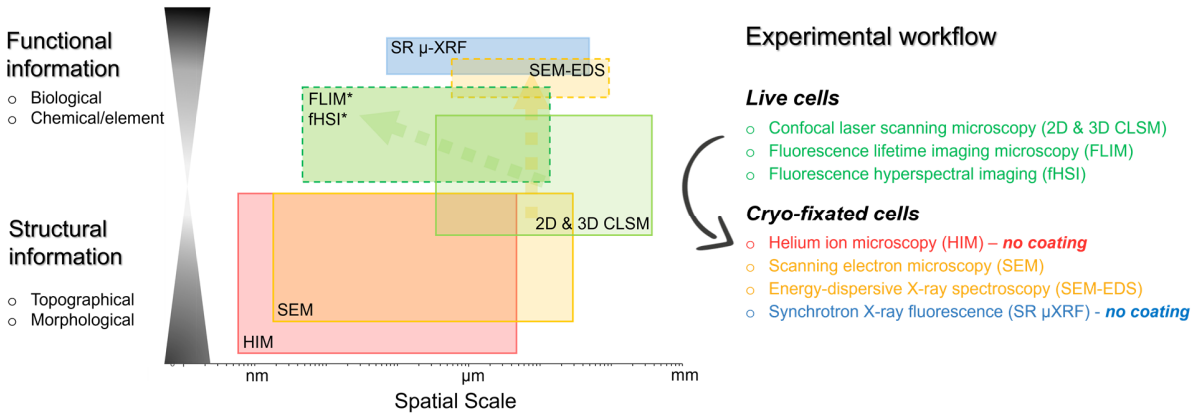

106

107 **Figure 1.** Novel multimodal microspectroscopy-based correlative microscopy enables a comprehensive
108 investigation of the studied nano-bio interface across a broad spatial scale, from tens of microns down to
109 the nanometer level. This approach provides both functional and structural insights, which in our study
110 focus on the interface between lung epithelial cells and exposed NMs. The colored areas illustrate the
111 typical imaging ranges for each technique, highlighting the type and extent of information obtained. * The
112 spatial resolution extends beyond the optical limit, as FLIM and fHSI can probe molecular interactions at a
113 sub-diffraction scale.

114

115 Results and discussion

116 Impact of TiO_2 NTs on DNA binding and the transport in apoptotic lung epithelial cells

117 To gain new insights into the response of lung epithelial cells to exposed metal oxide NMs, we
118 first performed an integrated multimodal high-resolution fluorescence imaging on live cells
119 exposed to TiO_2 NTs for two days with a meaningful surface dose (3 µg/cm^2), as discussed in

120 Supplementary Comment #1 (Figure 2A-B). Cells were grown on special, 10 nm thin Finder grid
121 Formvar/Carbon substrates, with fiducials used for correlative microscopy (Figure 2A, arrow).
122 Prior to measurement, the observed cell mitochondria, actin network, and nuclei were stained to
123 characterize any potential structural and/or functional changes that may have occurred as a result
124 of nanoparticle exposure. To track and determine potential co-localization between stained
125 cellular structures and nanoparticles, TiO_2 NTs were fluorescently labeled prior to administration
126 according to the well-established protocol.[48] To be able to successfully register and overlap the
127 correlated images by identifying the fiducials, we first applied low-magnification imaging (10X)
128 using two-channel confocal laser scanning microscopy (CLSM). In addition to clearly visualizing
129 the grid, used as a fiducial (Figure 1A, in black), it was possible to distinguish between TiO_2 (in
130 red) and mitochondria (in green). To delve deeper into the interaction between TiO_2 and cells, we
131 performed high-resolution imaging in three dimensions (3D) at 60X magnification (Figure 1A,
132 second image). The 3D image shows the localization and aggregation of TiO_2 on the cell surface
133 (white arrow), a phenomenon observed and described in our recent study.[39] Here, we further
134 unravel the high heterogeneity of the composites in morphology and size (upper image plane
135 (UP)). However, the similar excitation and emission profiles of the fluorescent dyes prevented a
136 clear differentiation between the TiO_2, nucleus and actin structures beneath the cell membrane
137 (lower image plane (LOW)), using a 2-channel CLSM.

138 To identify these individual structures, we proceeded with fluorescence lifetime imaging
139 microscopy (FLIM), integrated into the same experimental setup. FLIM, a powerful imaging
140 technique for measuring the lifetime of fluorescent molecules independent of signal intensity,[3]
141 also provides quantitative insights into the properties and dynamic changes of the surrounding
142 molecular environment[49] - an advantage we later utilized. With FLIM, we were able to identify the
143 individual labeled structures (Figure 2B), which was not possible with the 2-channel CLSM. The
144 fluorescence lifetime, as measured in each image pixel, is color coded with the mean lifetime (τ_m),
145 which is the weighted average of the individual lifetime components (τ_i) from the bi-exponential fit
146 (see Equation 1). The FLIM analysis, performed after using a single excitation laser (λ = 640 nm),
147 allowed to distinguish between actin structures (shown in blue), a nucleus undergoing a distinct
148 phase separation due to specific biophysical and/or biochemical processes[50] (shown in orange),
149 and TiO_2 with a wide τ_m distribution (shown in green to yellow). The latter indicates on a high
150 degree of structural and molecular variability and most likely local attachment of DNA molecules
151 and/or their fragments to the surface of nanoparticle composites (see the regions indicated by the
152 arrow). The proximity of the Draq5 dye, intercalated in the DNA structure at a distance of less

153 than 10 nm, to the Alexa Fluor 647 dye attached to TiO_2 plausibly induces a fluorescence
154 resonance energy transfer (FRET) transition, which is known to shorten the fluorescence decay
155 time.[51] This is evidenced by the blue shift in both the τ_1 and τ_2 distributions (Figure 2B, upper right
156 image). We also observed the Draq5 signal locally concentrated in the cell cytoplasm (see the
157 asterisk). With the additional experiments taking advantage of the combined FLIM and
158 fluorescence hyperspectral imaging (fHSI), we further confirmed the local and widespread
159 presence of DNA in the cytoplasm, apparently co-localized with the TiO_2 NTs (Figure S1),
160 suggesting a possible downstream inflammation.[52] These intracellularly formed nano-bio
161 composites may represent one of the key early states in the cell clearance mechanism that
162 evolves into the observed surface-immobilized TiO_2-bio composites.

163 To gain further insight into the structural and functional properties of the formed composites
164 in relation to DNA binding, we then prepared the samples for correlative SEM (Figure 2C). Due
165 to the chemical fixation treatment of 4% PFA and 2% GA and the fragile thin formvar/carbon
166 support films, we observed a slight displacement of the investigated cell and its structures as
167 indicated by the white arrow. However, this was not a limitation in this study, as the identification
168 of the same extracellular vesicles (EVs) in fixed cells was sufficient for subsequent morphological
169 and chemical characterization (Figure 2C-D). The SEM measurements revealed the presence of
170 distinct morphological features of large EVs that resembled apoptotic bodies (ABs).[53] Additional
171 SEM-EDS chemical mapping (Figure 2D) with typical spectra (Figure S2) revealed that rough
172 surface topography was co-localized with the presence of TiO_2 (Ti map in green), while all large
173 EVs exhibited a similar amount of organic matter (C map in yellow). Given that the electron
174 penetration depth and interaction volume for the detected characteristic X-rays are on the order
175 of a few microns at E_0 = 15 keV,[54] and considering the much thinner measured layer of organic
176 matter in EVs with a high nanoparticle content (Ti 23.8 wt%), we confirmed a concentrated
177 accumulation and extensive binding of organic matter (lipids and proteins) to the TiO_2 surface—
178 consistent with findings from our recent study.[55] Through detailed chemical analysis of the distinct
179 regions labeled 1-3 (Figure 2C), we confirmed previous FLIM-based observations suggesting the
180 very likely presence of DNA in EVs (Figure 2D). The weight percentage (wt%) of the elements
181 shown in the table and in the corresponding bar charts show a clear, more than threefold,
182 elevation of phosphate (P) and sodium (Na) inside EVs (sites 2 and 3) compared to the
183 surrounding cell membrane (site 1). The values are normalized to the concentration of organic
184 matter - in our case organic nitrogen (P/N and Na/N) – within each measured region to remove
185 the potential effects of different densities and interaction volumes, all of which affect EDS
186 detection. It is noteworthy that there was no discernible difference in P/N between EVs with high

187 and negligible TiO_2 content, indicating a similar concentration of DNA or its fragments in both cell-
188 excreted structures. However, the different morphologies of these large EVs, observed by both
189 high magnification SEM and FM on live cells, suggest on completely different functions and
190 modes of action for DNA loading, packaging and transport, all of which are considered essential
191 for cellular homeostasis and immune response modulation.[56]

192 The most likely cause of the high P accumulation in flat-surfaced EVs (site 2) is the high
193 concentration of DNA with associated binding proteins in the so-called plasma membrane
194 blebbing process, followed by its release from the cells in the form of apoptotic bodies, being the
195 largest class of EVs. This has the biological implication of impending apoptosis of the measured
196 cell, with the shape indicating still on an early stage of this process. However, the initiation of cell
197 apoptosis may well be indicated by the observed chromatin condensation, which is known to be
198 one of the sequences of nuclear changes culminating in cell apoptosis,[57] and the observed round
199 mitochondria, which are known to occur under conditions that compromise mitochondrial function,
200 such as cell apoptosis[58] (Figure 2A, see arrows in lower right image). On the other hand, the EVs
201 with a rough surface and a significant accumulation of TiO_2 appear significantly different from the
202 previously observed EVs, casting doubt on whether these structures are truly apoptotic bodies.
203 The most likely cause of the high concentration of organic phosphates (P), further supported by
204 the highest accumulation of mineral Na^+ among the measured sites, is a physical rather than a
205 biological mechanism, as previously reported.[59,60] Namely, the DNA phosphate backbone has
206 been found to play the major role in TiO_2 adsorption [59], while Na^+ has been found to preferentially
207 adsorb to the TiO_2 surface as inner-sphere complexes,[60] both under high ionic strength conditions,
208 [59] such as our cellular environment. Preferential DNA binding to TiO_2 surface, being found in both
209 cytoplasmic (Figure S1) and cell surface region (Figure 2), may have important biological
210 implications for disturbing cellular homeostasis. Interference with transcription or even replication
211 processes, as observed in our recent study,[41] may lead to genotoxic effects.[61] On the other hand,
212 Na^+ binding, if carried out intracellularly, could disrupt the ion homeostasis, leading to disruption
213 of membrane potential and the related processes. Moreover, the immobilization of TiO_2-rich,
214 irregularly shaped EVs, on the cell surface by the intertwined actin fibers from the inside (Figure
215 S3, super-resolution STED microscopy on live cells) and fibrin-like fibers from the outside reported
216 in Figure 5, could affect the normal clearance of apoptotic cells and potentially introduce
217 pathological conditions for the inflammation or autoimmunity.

218 To elaborate on this hypothesis, the observed, dense structure of immobilized EVs on the
219 apoptotic cell surface could partially block the secretion pathways of the typical anti-inflammatory

signals, thereby disrupting the typical anti-inflammatory environment. Moreover, if apoptotic cells are not cleared efficiently and in a timely manner by macrophages due to their overload in high particulate matter exposure and plausibly reduced motility,[62] they may progress to secondary necrosis and lose their membrane integrity.[63] By releasing immunostimulatory content or so-called damage-associated molecular patterns (DAMPs), the cellular dynamics then promotes inflammation and recruitment of immune cells. DAMPs are released through the lesions in the plasma membrane orchestrated by the plasma membrane protein Ninjurin-1 (NINJ1), which is structured into supramolecular filamentous assemblies as recently shown by super-resolution microscopy.[64] A meaningful observation is that the polymerized filaments range in size from a few tens to a few hundred nanometers—closely matching the dimensions of the lesions or holes we found on the cell surface close to the anchored TiO_2-rich excreted structures (Figure 3D). Thus, the holes may not necessarily be entirely a consequence of the incomplete sample preservation during cryofixation and freeze-drying, but may actually represent the plasma membrane lesions. However, further studies with better statistics are needed to confirm this.

Taken together, this provides an additional possible mode of action in the initiation of chronic lung injury—complementing the well-established mechanisms of PM- and TiO_2-induced macrophage phagocytosis dysfunction[65–67] and our recently discovered nanomaterial cycling between the lung alveolar surface and macrophagesl,[39] both of which lead to chronic inflammation.

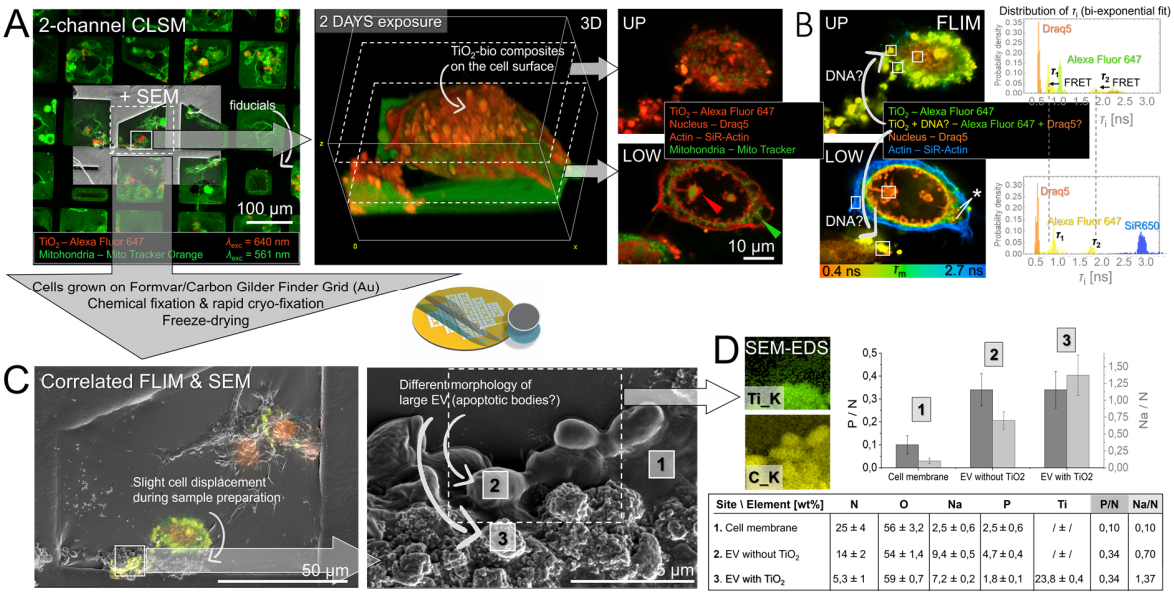

Site \ Element [wt%]	N	O	Na	P	Ti	P/N	Na/N
1. Cell membrane	25 ± 4	56 ± 3,2	2,5 ± 0,6	2,5 ± 0,6	/ ± /	0,10	0,10
2. EV without TiO_2	14 ± 2	54 ± 1,4	9,4 ± 0,5	4,7 ± 0,4	/ ± /	0,34	0,70
3. EV with TiO_2	5,3 ± 1	59 ± 0,7	7,2 ± 0,2	1,8 ± 0,1	23,8 ± 0,4	0,34	1,37

240 **Figure 2.** Correlative multimodal fluorescence microscopy and SEM-EDS (multimodal CLEM) applied on
241 lung epithelial LA4 cells exposed to TiO_2 NTs for 2 days reveals physico-chemical properties of the nano-
242 bio interface and the insights of DNA binding and transport during plausible cell apoptosis. A) Low to high
243 magnification 2D/3D CLSM showing TiO_2-bio composites on the cell surface and the morphology of the cell
244 nuclei, actin and TiO_2 (in red) and mitochondria (in green). B) The same structures with correlated FLIM
245 capable of precisely distinguishing between individual labeled structures (color coded from red to blue),)
246 using single laser source (λ = 640 nm). Shifted distribution of τ_1 and τ_2 from bi-exponential fit (green to yellow
247 in the chart on the right) indicate on local FRET between TiO_2 and DNA dyes, revealing plausible binding
248 of DNA to TiO_2 surface. C) Correlated FLIM and SEM after a successful registration and overlap of fiducials
249 shown in A). High magnification image reveals large EVs with different morphologies, denoted with 2 and
250 3. D) Chemical characterization of the same structures performed by SEM-EDS confirms not only high
251 accumulation of biological matter (C) on nanoparticles' surface (Ti), but also a few times higher content of
252 organic phosphate normalized to biological matter (P/N) (right chart and table) indicating a high but
253 mechanistically different DNA load inside large EVs.

254

255 **In-depth morpho-functional characterization of cell-excreted and surface-immobilized**
256 **TiO_2-bio composites**

257 To further investigate the morphological and structural properties of TiO_2-bio composites
258 immobilized on the cell surface, as well as to gain further insight into their chemical properties at
259 the sub-micron scale, we implemented an extended approach, a multimodal CLEM combined with
260 synchrotron μ-XRF (CLEM-μXRF), where we joined 2-channel CLSM, FLIM and fHSI on living
261 cells with SEM and μ-XRF on cryo-fixated cells (Figure 3). To improve the quality of the imaging
262 capability and sample preservation in our novel correlative microscopy pipeline, we used special
263 100 nm thick silicon nitride (Si_3N_4) substrates/windows (Figure 3A) that are transparent to soft X-
264 rays and avoided chemical fixation to preserve the nanoscale features of the investigated nano-
265 bio structures (Figure 3D), respectively. In order to improve the resolution and sensitivity of the
266 analysis of particularly light elements, we integrated spatially resolved synchrotron radiation SR
267 μXRF (Figure 3E-F), with its ability to achieve up to an order of magnitude better, sub-micron
268 spatial resolution and up to several orders of magnitude better elemental sensitivity[68] than SEM-
269 EDS, making it a valuable tool for investigating intricate biological processes such as ours.

270 Lung epithelial cells were grown on a surface modified Si_3N_4 substrate with fiducials in the
271 form of multiple 100 x 100 μm transparent windows and exposed to fluorescently labelled TiO_2
272 NPs for a period of 3 days. We observed a large number of TiO_2-rich structures, measuring up to
273 a few microns in size as shown in green and orange using a wide-field FM (Figure 3A) and

274 enhanced-resolution CLSM (Figure 3B), respectively. For visualization, the cells were stained with
275 the in-house synthesized lipid droplets (LDs) dye. Due to partitioning of the dye to other lipid-rich
276 environments during the incubation period, the contrast of the LDs was reduced, as shown by the
277 green color (Figure 3B). With CLSM, in comparison to a wide field FM, we were able to better
278 distinguish each of the numerous TiO_2 NTs-rich composites, which varied in size and shape.

279 To gain further insight into the local properties and interactions in the near molecular
280 environment of the observed TiO_2 NTs-rich structures and LDs, we performed FLIM and fHSI
281 imaging/mapping at the same site (Figure 3C). The typical and easily distinguishable FLIM and
282 fHSI spectra from the two distinct cell compartments within the white rectangles and
283 corresponding fits using a bi-exponential function (Equation 1) and an empirical intensity-
284 normalized log-normal function with nanometer peak position resolution,[69] respectively, are
285 shown in the top. The fHSI of LDs and lipid-rich regions showed spectral shifts of up to 10 nm,
286 ranging from λ_{max} = 660 nm (in purple) to λ_{max} = 670 nm (in blue), indicating local
287 microenvironmental differences, such as molecular conformation, polarity, etc.[70] This was
288 supported by FLIM data, with LDs showing a reduced mean fluorescence lifetime (τ_m) (lighter
289 blue) compared to other lipid-rich regions (darker blue), indicating an increased packing density
290 of the dye within LDs. The analysis of TiO_2 NPs-rich structures showed less heterogeneity, but
291 still with a considerable range in τ_m, ranging from 0.6 to 1.0 ns, also indicating on differences in
292 the packing density. An increased τ_m may also indicate a greater distance between fluorophores,
293 possibly due to lipid interspacing, as shown previously.[39]

294 To probe deeper into the properties and possible consequent effects of the TiO_2 NTs-bio
295 interaction, we introduced to our pipeline an additional correlated SEM and SR μXRF (Figure 3D-
296 E). The combination of these advanced techniques provided new insights into the morphological
297 and structural features well below the micron scale. The use of a 150 mM ammonium acetate
298 wash solution to remove buffer salt crystals, which otherwise interfere with structural and chemical
299 analysis,[71] followed by rapid cryofixation by plunge freezing and final lyophilization, allowed the
300 preservation of the majority of cell surface structures, including the studied TiO_2 NPs-rich excreted
301 composites studied (Figure 3D). The high magnification SEM image shows an almost perfect
302 spherical structure (indicated by the white arrow), likely resulting from the most efficient packing
303 of nanoparticles with the lowest surface energy-maximizing stability.[72] To confirm that the
304 structure is composed of nanoparticles, we observed strong co-localization with the fluorescence
305 signal of a TiO_2 dye, as measured by CLSM in live cells (Figure 3B, outlined in a rectangle). This
306 is further illustrated by the overlap of all correlated results from CLEM-μXRF in Figure 3G

307 (indicated by the arrows). To obtain further biological information on these intriguing structures
308 formed on the cell surface, the same sample was transferred to a synchrotron facility for the
309 elemental mapping using SR μXRF (Figure 3E), supported by scanning transmission X-ray
310 microscopy (STXM) (Figure 3F) for simultaneous mapping of atomic number by absorption
311 contrast sensing.[68] The spectral maps of primarily light elements have been generated from the
312 spectral data and their fits, where we show an example from the site marked with an asterisk. The
313 color-coded theoretical spectra for each of the measured elements fit perfectly to the raw data (in
314 black) with a high signal to noise ratio (S/N) due to the high detection sensitivity of the technique.
315 The results confirm not only a high TiO_2 content within highly spherical composites, as evidenced
316 by locally elevated concentrations of O (K-shell emission spectra) and Ti (much weaker L-shell
317 emission spectra), but also a higher content of C, N, Mg and, to some extent, Na (all K-shell
318 emission spectra) at the same locations. This again confirms the extensive physical affinity of
319 biomolecules, such as lipids or cholesterol, shown previously[39] and positive ions to the surface of
320 the TiO_2 NTs as elaborated in the first results section. It further validates and signifies our recent
321 findings performed on the same nano-bio system using a combination of omics, *in vitro*
322 measurements and full-atom *in silico* simulations, which reported strong interaction of amine and
323 phosphate groups of the disordered lipids with the TiO_2 NTs surface.[39] Extensive biomolecule
324 binding, forming the so-called lipoprotein corona as clearly demonstrated by the ultra-high
325 resolution imaging (Figure S4), can significantly disrupt cellular homeostasis by altering protein
326 function, affecting cell signaling and trafficking machinery,[73] all of which can potentially lead to
327 immune activation and long-term cellular stress. The local increase in Na^+ adsorption may be due
328 to the high surface/volume characteristic of anatase TiO_2 NTs, allowing Na^+ to intercalate into the
329 surface and subsurface layer.[74] The most interesting observation is the deviation of the
330 distribution of plausibly extracellular Na^+ from the rest of the elemental maps, indicating at least
331 partially a different binding mechanism. Using correlated μXRF and SEM, we observe complete
332 co-localization of the highly elevated Na^+ sites with the distinct filamentous structures formed by
333 cells bridging the TiO_2-bio composites (Figure 3E, bottom image, purple arrows). Good correlation
334 of chemical maps with distinct physical properties not only highlights a fundamental link between
335 composition and structure, but also suggests a potential functional relationship. The preferential
336 binding is likely due to the high concentration of negatively charged biomolecules within the
337 filamentous structure. Among these, heparan sulfate (HS) chains stand out, as they possess the
338 highest negative charge density of any known biological macromolecule and are commonly found
339 on cell surfaces.[75] These molecules also play a central role as mediators in inflammatory
340 processes,[76] suggesting local inflammatory activity on TiO_2-bio composites bridged with these

filamentous structures. In addition, the sequestration of both intrinsic and/or extracellular Na^{+} and Mg^{2+} may result in alteration of ion homeostasis, disruption of normal associated cellular functions and induction of oxidative stress.

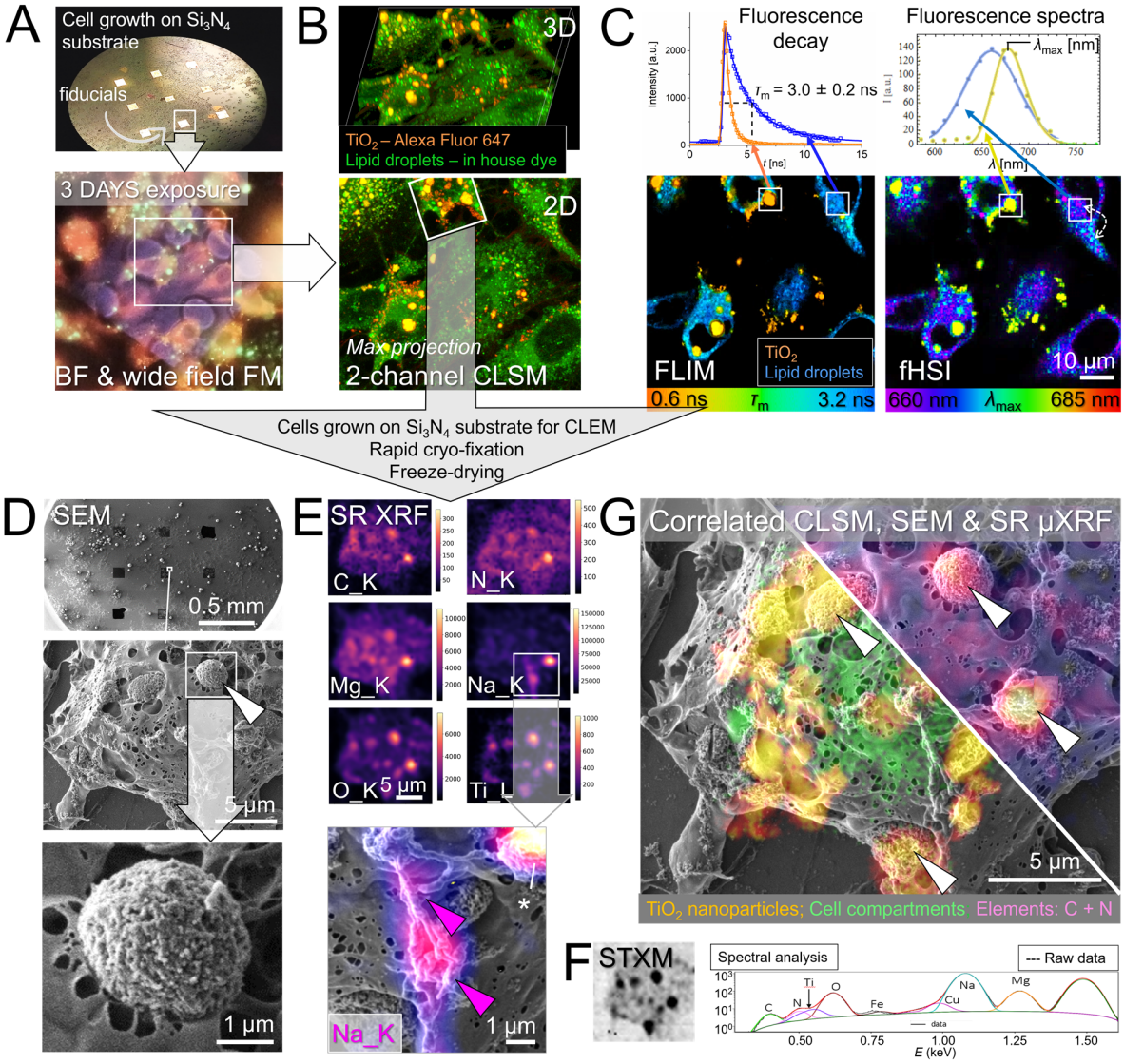

Figure 3. Novel multimodal CLEM combined with synchrotron µXRF (CLEM-µXRF) revealing in-depth physico-chemical and morpho-functional properties of inflammatory TiO_2 NPs-rich cell-excreted composites immobilized on the surface of lung epithelial LA4 cells. A) Combined BF and wide field FM employed to visualize cell growth on 100 nm thick transparent silicon nitride (Si_3N_4) films of the 100*100 um dimension used as fiducials and optimal substrate for the correlative microscopy both reflection and transmission mode (µXRF). B) 2D and 3D CLSM performed on the same site to show labeled cells (in green) and cell-excreted TiO_2 composites (in orange) with an improved resolution. C) The same site characterized with additional

352 FLIM and fHSI, capable of distinguishing between individual labeled structures and of inspecting local
353 microenvironment differences, such as molecular conformations or polarity. The upper charts illustrate FLIM
354 decay curves and fluorescent spectra for the two distinct sites. D) Low to high magnification SEM images
355 of the same site performed after rapid cryo-fixation of the sample to preserve distinct structural features of
356 the TiO_2-bio composites on the cell surface (bottom image). E) SR μXRF elemental maps from the same
357 site showing the extensive binding of intrinsic biomolecules (C and N) and essential minerals (Na^+ and
358 Mg^{2+}) on the TiO_2-rich local sites. High-magnification correlated Na^+ map and SEM further highlighting very
359 likely functional relationship between composition and filamentous structure with potential inflammatory
360 implications. F) Supporting atomic number (Z) and density-sensitive STXM map with the typical XRF
361 spectra collected from the TiO_2-bio composite site (denoted with an asterisk) and its color-coded fits for
362 individual elements. G) Correlated live cell CLSM and high-vacuum SEM and μXRF revealing morpho-
363 functional properties on the distinct sites (white arrows).

364 To further elucidate the intricate morpho-functional properties of the studied nano-bio interface
365 at the nanoscale, we correlated multimodal CLSM with SR μXRF and ultra-high resolution helium
366 ion microscopy (HIM), performed for the first time (Figure 4).

367 By targeted fluorescence labelling prior to live cell imaging of lung epithelial LA4 cells, that
368 had been exposed to TiO_2 NTs for a period of 2 days, we were able to perform a detailed
369 characterization of highly specific nano-bio structures formed on the cell surface (Figure 4A-B).
370 Again, a large, condensed TiO_2 NTs-biostructure, up to a few microns in size, with an
371 approximately spherical shape, was observed and imaged in detail in the multichannel 2D and
372 3D (Figure 4A). Moreover, we performed additional FLIM and fHSI imaging (Figure 4B), which
373 allowed us to investigate the potential heterogeneity of the molecular environment in the
374 immediate vicinity of the reporting fluorophores attached to the surface of TiO_2 NTs. While fHSI
375 showed no significant spectral variation across the composites, indicating the absence of any
376 particular local molecular and physical changes in the immediate nm vicinity, FLIM, revealed
377 significant deviations in the fluorescence lifetimes (τ_m) within the same locations, as indicated by
378 the orange and blue rectangles. This may be indicative of different degrees of dye
379 aggregation/self-quenching[77] due to the different surrounding molecular environment, but a more
380 in-depth investigation using an expanded set of complementary techniques, is required to better
381 understand the cause.

382 To elucidate the underlying cause of the observations, the sample, grown on Si_3N_4 substrate
383 was cryo-fixated immediately after fHSI/FLIM imaging and transferred to successive correlated
384 high-vacuum SR μXRF and ultra-high resolution HIM for the most accurate chemical and
385 morphological analysis, respectively. Chemical speciation and detailed surface examination

386 provided new insights that now better explain the differences in the molecular environment
387 observed in living cells (Figure 4C-E). Using extremely sensitive, sub-micron resolution SR μXRF,
388 we revealed the presence of localized, highly concentrated iron (Fe) (indicated by the dashed
389 rectangle), as opposed to more widely distributed titanium (Ti), and in particular intrinsic carbon
390 (C) and oxygen (O). By superimposing the data from all three complementary techniques (Figure
391 4E, on the right), we observe a remarkable co-localization of the concentrated Fe (in pink),
392 reduced fluorescence lifetime (in orange), supported by the distinct morphological and
393 topographical feature within the same region provided by ultra-high resolution HIM (Figure 4C,
394 left inset). With our novel correlative microscopy approach, we not only identified a close
395 relationship between FLIM footprint, Fe content and distinct surface morphology, but also gained
396 a better morpho-functional assessment of the observed nano-bio structure to better elucidate
397 possible causes and consequent biological effects, as discusses here.

398 The site of highly localized Fe, accompanied by the numerous distinct morphological features
399 at the outer edge, suggesting possible biological transport channels in the form of tunneling
400 nanotubes (TNTs)[78] with an average diameter of 50 nm (Figure 4C, marked with arrows), implies
401 the biological cause of its accumulation through the active cell secretion. This also implies the
402 nanoparticle-induced alteration of iron homeostasis and the subsequent cell-protective
403 mechanism, through the initiated cellular iron efflux, plausibly via the major iron transporter
404 ferroportin (Fpn).[79] This mechanism opts to mitigate iron-induced reactive oxygen species (ROS)
405 and pro-inflammatory cytokine production and further iron-mediated inflammation that can
406 damage DNA, proteins and lipids.[80] The remaining question is, why the accumulation in the TiO_2-
407 bio composite? These large TiO_2-rich extracellular vesicles may serve as extracellular containers
408 for the other waste molecules, where their high absorptivity at the metal oxide surface, such as
409 ferrous iron,[81] may also play an important role.

410 To better understand the physical aspects of the interaction, we need to understand the
411 corresponding reduced fluorescence lifetime of the biological molecules present at the nano-bio
412 interface. The proximity and/or adhesion of Fe particles to the TiO_2 surface could potentially
413 induce a phenomenon of localized surface plasmon resonance (LSPR)[82] resulting from the laser-
414 induced collective oscillations of surface electrons in a conduction band,[83] leading to a shorter
415 fluorescence lifetime.[84] Conversely, Fe could interact with nearby lipids and proteins enveloping
416 TiO_2, catalyzing lipid peroxidation,[85] inducing lipid bilayer disruption through an increase in water
417 permeability and thus an increase in membrane polarity,[86] resulting in a shortening of the dye
418 lifetime.

The implementation of correlative ultra-high resolution and large depth-of-field HIM revealed another intriguing feature at the center of the object, resembling a 'wormhole' (inset on the right). The more than 1 µm deep void, or tunnel, was formed during the assembly of a TiO_2-bio composite and could potentially be used for the diffusion and selective matter exchange between the inside and outside of the cell. This type of nano-bio interface assembly with the revealed nm features has never been demonstrated before and could be an interesting subject for further studies.

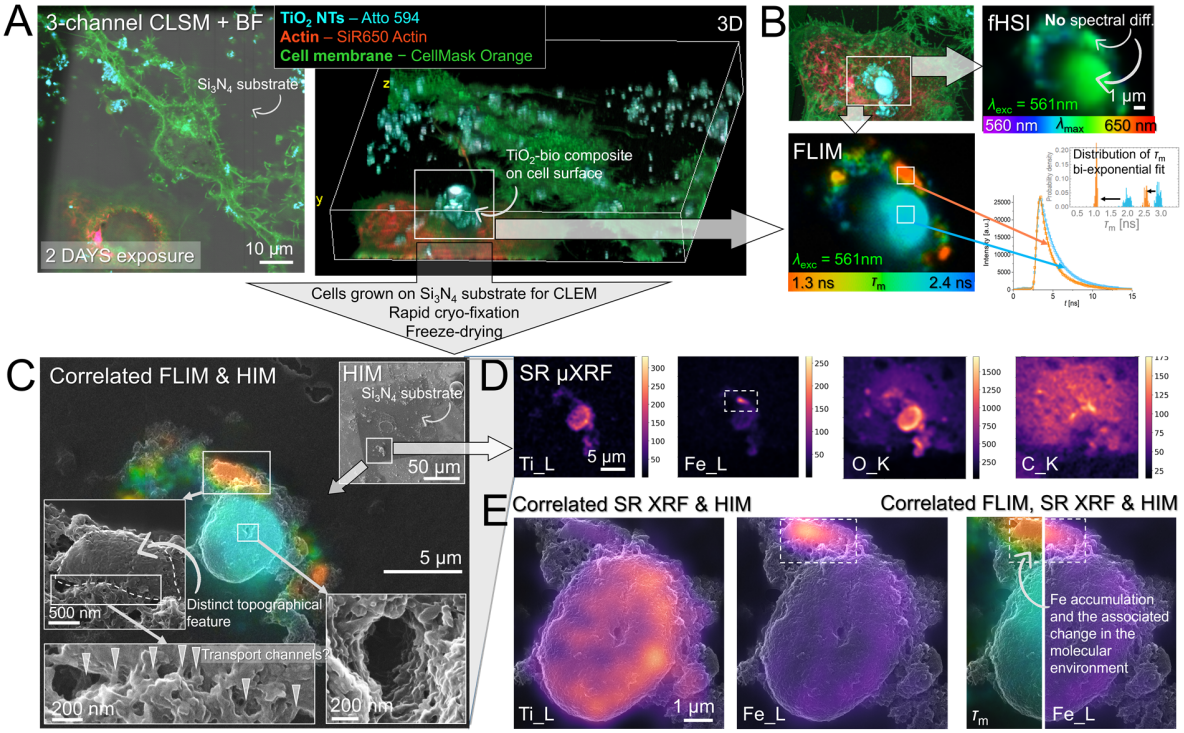

Figure 4. Novel correlated high-resolution FLIM, SR µXRF and HIM providing in-depth morpho-functional assessment of inflammatory TiO_2-bio cell-excreted composites immobilized on the surface of lung epithelial LA4 cells. A) Cells grown on thin Si_3N_4 transparent substrate (in gray, BF image) with labeled cell membranes (in green), actin (in red) and nanoparticles (in light blue) acquired with 3-channel CLSM using 60X water immersion objective. 3D CLSM revealing size, shape and topography of a large, few micron-sized TiO_2-bio composite formed on the cell surface (marked with an arrow). B) fHSI and FLIM imaging and analysis of the investigated structure uncovering no particular spectral, but significant fluorescence lifetime contrasts, respectively (see the charts on the right). C) Correlated FLIM and HIM exhibiting co-localization of distinct fluorescence lifetime map (in orange) and nanoscale topographical features marked in the left inset image. Further ultra-high magnification inset images on the bottom uncover intriguing morpho-functional features, from the apparent multiple transport channels into the local site with an accumulated

438 Fe (marked with arrows) to the void or tunnel formed in the center of the TiO_2-bio composite extending
439 towards the plasma membrane. D) SR μXRF elemental maps of metals and biomolecules distributed locally
440 and more evenly throughout the investigated cellular region. E) Changes in physical properties of the
441 molecular environment on the nano-bio interface plausibly caused by high Fe accumulation shown by
442 correlated FLIM, SR μXRF and HIM, the correlative microscopy approach applied for the first time.

443 Finally, we uncover one of the potentially crucial initiating modes of action in the inflammatory
444 cell response to TiO_2 NTs. Using high magnification SEM, we have observed and characterized
445 a thin fibrous network of biological material that has developed locally over a large TiO_2-bio
446 composite immobilized on the cell surface (Figure 5D). The organization and the thickness of the
447 fibers of a few tens of nanometers are reminiscent of fibrin.[87,88] Considering that fibrin has been
448 found to be excessively deposited in the early stages of acute intra-alveolar lung injury,[89,90]
449 plausibly accompanied by the secretion of fibrinogen by lung epithelial cells,[91] the possible
450 presence of fibrin on our studied nano-bio interface could have significant biological implications
451 for the local pro-inflammatory stimuli accompanied by the secretion of cytokines, such as tumor
452 necrosis factor (TNFα).[92] To better elucidate the possible TNFα secretion-induced fibrin fiber
453 formation, we performed an additional TiO_2 NTs exposure experiment on the co-culture of lung
454 epithelial LA4 and murine alveolar macrophages MH-S, which are known to release TNFα after
455 exposure to metal oxide nanoparticles[93] or high aspect ratio nanomaterials[94] such as ours. Our
456 aim was to determine whether the presence of MH-S increased the formation of fibrous structures
457 locally on the TiO_2 NTs. The results reveal a significantly higher presence of fibrous structures on
458 nearly all TiO_2 NTs immobilized on the lung epithelial cell surface in the co-culture, compared to
459 the partial—yet still substantial—formation observed in the monoculture, primarily over the larger
460 composites (Figure S5). We also observe an extensive apical MH-S scavenging and uptake of
461 TiO2 NTs (Figure S6), where rounded macrophages with phagocytic protrusions capture and trap
462 the nanoparticles, identified by the white image contrast.

463 To confirm that the fibers consist of inflammation-mediating fibrin molecules, we performed
464 another correlative experiment by introducing labeled fibrinogen to the living cells exposed to TiO_2
465 NTs, allowing us to assess potential co-localization with the fibrous structures using the following
466 high-resolution HIM (Figure S7). Despite the much lower resolution of the confocal microscopy
467 images and the slight sample displacement during sample preparation, preventing the precise
468 registration and overlap with HIM, the results still show a good co-localization of the fibrous
469 network with the labelled fibrinogen, further supporting our hypothesis. To further explore the
470 potential of long-term inflammation and fibrogenesis in the development of such structures over
471 time, further studies are needed.

In addition to the fibrous structures observed by high magnification SEM and HIM, we provide a correlative characterization of the same TiO_2-bio composites using multimodal live cell 3-channel CLSM and FLIM (Figure 5A-B) and SR µXRF (Figure 5E-F). FLIM revealed a high degree of heterogeneity in the fluorescence lifetimes of Atto 594 dye attached to TiO_2 NTs. The average lifetime τ_m, calculated from a bi-exponential fit, was approximately half shorter in localized regions (in yellow) than in the rest parts of the sample (in green to blue). Correlated SR µXRF again showed a co-localization between the short fluorescence lifetime and the site with high Fe accumulation (Figure 5E-F) as reported in Figure 4, suggesting a similar underlying mechanism.

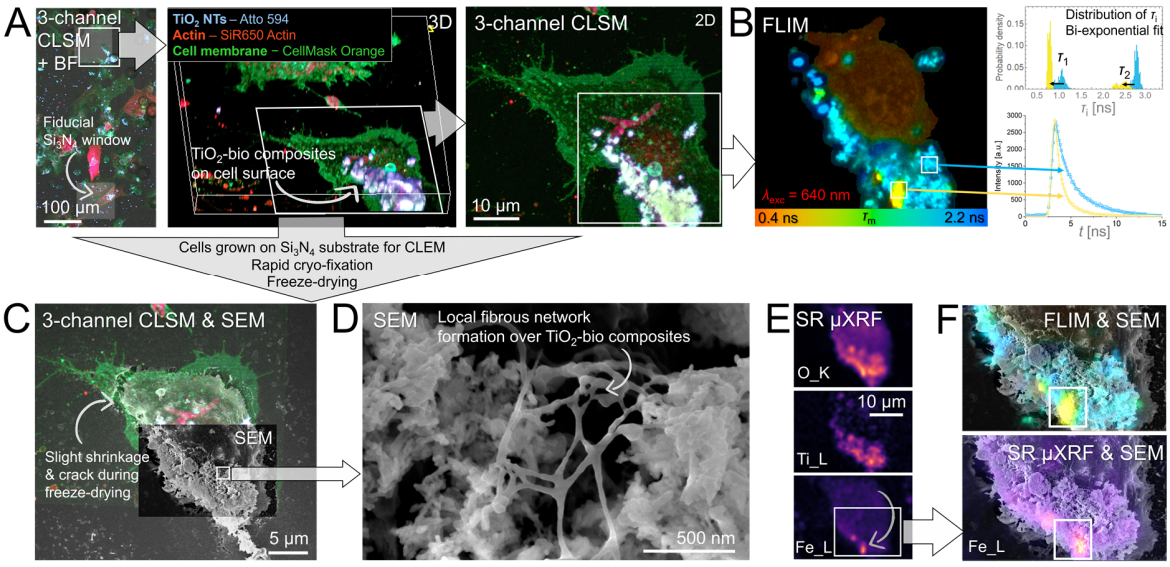

Figure 5. Novel high-resolution CLEM-µXRF confirming Fe-induced changes in the physical properties of the surrounding biological environment and uncovering the plausible inflammatory local formation of fibrous network resembling fibrin matrix formed over TiO_2-bio composites immobilized on the plasma membrane of lung epithelial LA-4 cells. A) Cells grown on thin Si_3N_4 substrates (in gray) with labeled cell membranes (in green), actin (in red) and nanoparticles (in blue) acquired with 3-channel CLSM using 10X and 60X objective magnification. High-magnification 2D and 3D CLSM reveal size, shape and topography of a large, more than ten micron-sized TiO_2-bio composite arrested on the surface (marked with an arrow). B) FLIM imaging (on the left) and analysis (on the right) of the investigated composite revealing significant contrast in fluorescence lifetime between local regions (from yellow to blue). C) Correlated CLSM and SEM showing slight shrinkage and local cracks near the cell boundary after rapid freeze-drying but, most importantly, preserving the investigated structures on cellular surface. D) High-magnification SEM uncovering local formation and the morphology of fibrous network formed over the TiO_2-bio composites on the cellular surface, with its inflammatory implications further examined in the supporting Figures S4-5. E) SR µXRF elemental maps of metals and oxygen distributed throughout the investigated cell. F) Confirmation of Fe-

495 induced local physical changes on the nano-bio interface (inset regions) measured by correlated FLIM and
496 SR µXRF represented on the top of SEM data.

497

498 **Conclusion**

499 In this study, we highlight the importance of implementing novel multimodal and multiscale
500 extended CLEM, to elucidate the intricate interactions between biological matter and
501 nanoparticles. In particular, we present different response mechanisms of lung epithelial cells, a
502 subject of persistent exposure to particulate matter, to exemplary high aspect ratio TiO_2
503 nanotubes with known subacute and even chronic inflammatory inducing effects. The study
504 provides a comprehensive morpho-functional assessment of the nanoparticle-cell interface from
505 the micron down to the nanoscale with the implications for lung epithelial toxicity through the
506 uncovered possible initiating modes of action as schematically summarized in Figure 6. With the
507 novel correlative microscopy approach and in-depth analysis, we were able to advance the
508 understanding of the recently reported TiO_2-induced mechanism of chronic inflammation[39] and
509 genotoxicity[41] by better elucidating several possible cell response mechanisms to the disruptive
510 nature of this particular nanoparticle with different inflammatory and anti-inflammatory outcomes:

511 - Nearly spherical TiO_2 NTs-bio composites with extensive DNA binding immobilized on the
512 cell surface, similar to immobile apoptotic bodies, may result in defects in apoptotic cell
513 clearance. This may lead to secondary necrosis, loss of membrane integrity and release
514 of immunostimulatory contents through the observed plasma membrane lesions.
515 - The formation of distinct filamentous structures bridging TiO_2-bio composites, perfectly co-
516 localized with high Na^+ accumulation, indicating a localized, highly negative charged
517 surface of plausible heparan sulfate, a key mediator in cell inflammation.
518 - Nanoparticle-induced alteration of iron homeostasis and balance of other TiO_2-adherent
519 cellular compounds/biomolecules, followed by the controlled release of an excess iron or
520 other exchange compounds through transport channels, suggesting a cell-protective
521 mechanism.
522 - The localized formation of a fibrin-like fibrous network over TiO_2-bio composites indicating
523 on the local pro-inflammatory stimuli accompanied by plausible secretion of fibrinogen and
524 TNFα cytokines.

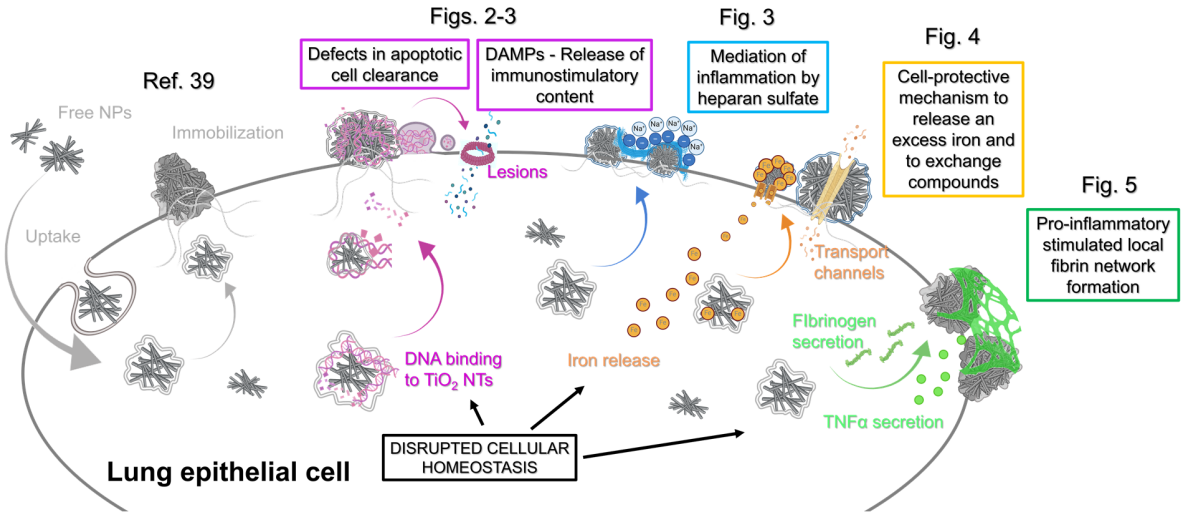

Figure 6. The schematic overview of the possible modes of action of the cell response to the disruptive nature of TiO_2 NTs, toxic to lung epithelial cells, with different inflammatory and anti-inflammatory outcomes (colored from pink to green), observed at the nano-bio interface.

By implementing such a multimodal and multiscale correlative microscopy approach for the first time, we were able to study and characterize the initial cellular responses to exposed nanoparticles at such a small scale. These responses may play a critical role in the body's initial immune response and the development of inflammation.

This methodology provides a strong basis for advancing research into the toxicity of nanoparticles and their potential impact on human health. By providing a robust framework, it enables further exploration and refinement of approaches to toxicity assessment. However, to fully realize its potential and guide future research, it is essential to address certain limitations. Key challenges include the limited high-throughput imaging required for improved statistics, together with faster acquisition to minimize sample displacement, and the need for optimization and better control of all physical variables throughout sample preparation to preserve nanoscale features throughout the sample. Both of these challenges point to better automation, which is discussed in Supplementary Comment #2 in the Supporting Information Appendix. This will lead to critical improvements in the future for more precise 2D/3D visualization, evaluation and deeper insights into nano-bio interactions and the mechanisms behind them, paving the way for more accurate and reliable interpretations of how different nanoparticles and their properties affect relevant biological systems, important for improved safety assessment.

546 ## Experimental section

547

548 ### Material

549 The murine epithelial lung tissue cell line (LA-4, ATCC CCL-196), murine alveolar lung
550 macrophage cell line (MH-S; ATCC, CRL-2019), F-12K medium (Gibco), Fetal bovine serum
551 (ATCC), 1% Penicillin-Streptomycin (Sigma), 1% non-essential amino acids, L-glutamine, beta-
552 mercaptoethanol (Gibco), Phosphate buffer saline (PBS), Live Cell Imaging Solution (LCIS,
553 Invitrogen); Titanium dioxide nanotubes (TiO_2 NTs) in anatase form synthesized in-house[95]; µ-
554 Slide 8-well (Ibidi), Silicon Nitride Si_3N_4 Support Film (PELCO, 21509CL, Ted Pella), TEM
555 formvar/carbon film on Au Gilder 200 F1 finder grids (FCF200F1-AU-50, EMS), Ammonium
556 acetate (Sigma-Aldrich), PTFE coated high precision and ultrafine tweezers (72919-3SATe,
557 EMS), propane transfer system for plunge freezer (37015, Electron Microscopy Sciences);
558 AlexaFluor 647 (Thermo Fischer Scientific), Atto 594 (ATTO-TEC), CellMask Orange (Invitrogen),
559 SiR-actin (Spirochrome), Draq5 (Invitrogen), MitoTracker™ Orange CMTMRos (Invitrogen),
560 PSM-39 (in-house).

561 ### Cell culture

562 The LA-4 murine epithelial lung tissue cells were cultured in 75 cm² TPP cell culture flasks. They
563 were maintained in a controlled environment at 37°C with 5% CO_2 and humidity using F-12K
564 medium supplemented with 15% fetal bovine serum (FBS), 1% penicillin-streptomycin, 1% non-
565 essential amino acids and 2 mM L-glutamine The MH-S alveolar macrophage cells were cultured
566 in RPMI 1640 medium (Gibco), supplemented with 10 % FBS, 1% penicillin-streptomycin, 1%
567 non-essential amino acids, 2 mM L-glutamine and 0.05 mM beta-mercaptoethanol (Gibco). Upon
568 reaching 70-90% confluency at the appropriate passage, the LA-4 cells were seeded onto
569 specially designed imaging holders customized for correlative microscopy. To enable both,
570 reflection and transmission imaging modes, thin Silicon Nitride (Si_3N_4) and formvar/carbon on Au
571 Gilder 200 F1 finder grid support films were used. For co-culture experiments, LA-4 and MH-S
572 were grown in separate dishes up to 70-90% confluency and mixed together by the ratio LA-
573 4:MH-S, 40:1. After 24h incubation, the co-cultures were exposed to nanoparticles for the desired
574 amount of time, prior microscopy. Growth medium in the co-culture was an equal mixture of F-
575 12K and RPMI 1640.

576 ### Nanoparticles

577 TiO_2 nanoparticles have been selected for investigation in this study due to the potential risks to
578 human health associated with inhalation or oral exposure.[96,97] In case of their high specific surface
579 area, recent studies have demonstrated the potential for these nanoparticles to elicit an
580 inflammatory response [39,40] and to possess carcinogenic properties.[41,98] TiO_2 nanotubes (TiO_2
581 NTs) in anatase form synthesized in-house with the protocol described in [95] exhibited a diameter
582 range of 6 to 11 nm, a mean length of 100-500 nm, and a BET surface area of 150 m^2 g^{-1}.[40] In
583 order to facilitate enhanced visualization and monitoring of nanomaterial interactions and their
584 impact on model lung epithelium at the sub-micron scale, the TiO_2 NTs were functionalized with
585 super-resolution compatible fluorescent probes, AlexaFluor 647 and Atto 594, according to the
586 protocol avoiding the introduction of artefact as described in [48]. Functionalized and filtered
587 nanoparticles suspension was stored in a 100-fold diluted bicarbonate buffer (5 mOsm L^{-1}) prior
588 administration to cells.

589 **Sample preparation for live-cell confocal fluorescence microscopy**

590 After reaching 70-90% confluency in culture flasks, LA-4 cells were reseeded directly onto UV-
591 sterilized Si_3N_4 or formvar/carbon Au finder grid substrates/holders placed within the chamber of
592 a µ-Slide 8-well. The volume of the added cell suspension prepared at a concentration of a few
593 10^5 cells/ml was 20 µl and resulted in approximately 5,000 cells per holder with a diameter of 3
594 mm. Following a four-hour period during which sufficient cell attachment to the substrate had
595 occurred, cell growth media was added to each chamber in order to cover the surface and wet
596 the entire holder, thus preventing any evaporation during the course of the measurements. Once
597 the desired confluency of approximately 50% had been reached (typically within two days), gently
598 sonicated (Bransonic ultrasonic cleaner, Branson 2510 EMT) nanoparticle suspension and
599 carefully rinsed onto the cell monolayer at an average calculated surface dose of 5:1
600 ($S_{nanomaterial}$:S_{cells}) and total 3 µg/cm². It presents a meaningful concentration according to the
601 lifetime occupational exposure and the safety recommendations as further discussed in
602 Supplementary Comment #1. The surface dose was achieved by pouring V = 5 µl of a suspension
603 of nanoparticles (c = 0.5 mg/ml) into the chambers of 1 cm² size filled with the cell growth media
604 (V = 300 µl). To put into perspective, the surface dose, which is the most important determinant
605 in the nanomaterial toxicity in lungs,[99] was used to be equivalent to exposure over a period of 45
606 working days, based on the 8-hour time-weighted average occupational exposure limit for TiO_2
607 (6.0 mg/m^3 TiO_2) established by Danish Regulations.[100] The cells were exposed to nanoparticles
608 for the desired period of time, which was one to three days, prior to live-cell imaging and following
609 cryopreservation for high-vacuum imaging.

610 Before live-cell imaging, cells were stained with different highly-specific fluorescent dyes to
611 visualize different cell compartments potentially interacting or responding to exposed
612 nanoparticles. Staining was performed according to the manufacturer's recommendations to
613 achieve sufficient fluorescent signal while preserving cellular functions. SiR Actin dye in
614 concentration c = 400 nM was used for 4 h to stain F-actin. Draq 5 dye in concentration c = 5 μM
615 was used for 15 min to stain double-stranded DNA. CellMask Orange in 1000X diluted stock
616 concentration was used for 10 min to stain cell plasma membrane. Mitotracker Orange in
617 concentration 500 nM was used for 15 min to stain mitochondria. All staining solutions were
618 removed and sample was rinsed a few times with LCIS prior measurements performed on the
619 microscope inside the stage top incubator with a temperature, gas and humidity control (H301-
620 MINI, Okolab). Before measurements, the implemented holders with the adhered cells were
621 flipped to enable imaging with small working distance (high numerical aperture) objective.
622 Sterilized polystyrene microspheres of 20 μm in size were employed as volume spacers in order
623 to prevent any compression of the sample.

624 **Sample preparation for high-vacuum electron and ion microscopy**

625 Immediately after live-cell imaging, sample was carefully transferred from the measuring μ-Slide
626 8-well into the 150 mM ammonium acetate washing solution to eliminate buffer salt crystals, which
627 otherwise interfere with both structural and chemical analysis performed with high-vacuum
628 techniques.[71] After few seconds of immersion in the washing solution for three times, an excess
629 of water was removed by careful blotting the sides of the sample holder with a lint-free paper.
630 Immediately after blotting, samples were rapidly cryofixated without chemical fixation, to preserve
631 the integrity and morphology of cellular structures and interacting nano-bio interface on the
632 nanoscale, using plunge freezing in a liquid propane to prevent the formation of crystalline ice[101]
633 and stored in a cryo bank until the final drying procedure in a freeze dryer (Coolsafe 100-9 Pro).
634 Propane was prepared in a liquid nitrogen-cooled chamber with the plunge freezer transfer
635 system. To carefully handle with the fragile specimens, high precision cryogenic and non-sticking
636 PTFE tweezers were used. In case of chemical fixation, ammonium acetate washing solution was
637 changed with 4% paraformaldehyde (PFA) and 2% glutaraldehyde (GA) solution. Samples were
638 fixated for 15 minutes at room temperature before blotting and rapid cryofixation.

639 **Confocal laser scanning microscopy (CLSM)**

640 The experiments were conducted on a custom-built inverted microscope (Olympus IX83, Abberior
641 Instruments). Imaging was conducted with Olympus 10x (NA = 0.3) and 60x (NA = 1.2) water

642 immersion objectives, utilizing two pulsed ps lasers in conjunction with a fast-gating system, which
643 was controlled by an FPGA unit. In order to facilitate the simultaneous detection of the
644 fluorescence emitted by different fluorophores, two pulsed diode lasers were employed, with
645 wavelengths of 561 nm and 640 nm, respectively, and a pulse length of 120 ps and repetition rate
646 of 80 MHz. Fluorescence was detected in a descanned mode using an additional pinhole to
647 reduce out-of-focus light and avalanche photodiodes (APD, SPCM-AQRH, Excelitas) with a
648 photon detection efficiency (PDE) exceeding 50% across the entire visible spectrum.
649 Fluorescence was collected from each scanning voxel using a dwell time of 10 µs and detected
650 within the spectral windows λ = 580 - 625 nm and λ = 650 - 720 nm, utilizing dichroics and band-
651 pass filters (both Semrock). For more comprehensive illustration of the optical setup, please refer
652 to the schematics in Figure S8. Supporting high-resolution measurements on live cells were
653 conducted with the integrated customized super-resolution microscopy (STED), using depletion
654 laser wavelength 775 nm, pulse length of 1.2 ns and the power of 200 mW in the sample plane.

655 **Fluorescence lifetime imaging microscopy (FLIM) and fluorescence hyperspectral imaging**
656 **(fHSI)**

657 The microscope system was upgraded with the 16-channel Multi-Wavelength Photo-Multiplier
658 Detectors (PML-16 GaAsP, Hamamatsu), a multi-dimensional Time Correlated Single Photon
659 Counting (TCSPC) detection system and a DCC-100 detector controller card (all manufactured
660 by Becker&Hickl), all communicated through fast ps FPGA electronics, enabling the simultaneous
661 detection of signals across up to 16 spectral channels and detection of their corresponding
662 fluorescence lifetime decays.[102] For fluorescence lifetime imaging, the signals collected on the 16
663 GaAsP detectors that arrived in the same time interval were summed and the FLIM decay curves
664 obtained in each pixel of the image analyzed using the SPCImage5.0 software (Becker&Hickl) as
665 done before.[103,104] The analysis of FLIM decay curves was conducted using a two-component,
666 double exponential fitting method convoluted with the instrument response function (IRF), which
667 constrains the achievable resolution to its 200 ps FWHM. The pixel exposure time (100 µs) and
668 image binning (3x3) were set to obtain a sufficient peak value of the decay curves of at least 1000
669 to eligibly resolve fitting with a double-exponential model:

$$I(t) = a_1 e^{-t/\tau_1} + a_2 e^{-t/\tau_2} \quad (1)$$

670

671 with the lifetime values of the fast and slow decay components, τ_1 and τ_2, and the corresponding
672 intensity coefficients, a_1 and a_2. The fitted FLIM decay curves from each pixel were color-coded

673 according to the average fluorescence lifetime $\tau_m = a_1\tau_1 + a_2\tau_2$, with the fastest decays shown in
674 red and longer decays in blue. Furthermore, fHSI was conducted utilizing 16 spectral channels
675 within the wide spectral window spanning from 560 nm to 760 nm, as determined by the diffraction
676 grating positioning within the spectrograph (PML-Spec, Becker&Hickl). The high quantum
677 efficiency of approximately 50% across the whole visual spectrum was achieved by GaAsP PMT
678 detectors. The total number of photon counts collected on TCSPC for each pixel was calculated
679 for each spectral channel and represented in the spectral curve. To avoid partial blocking of
680 photons on the notch filters in our de-scanned detection setup which distorts the acquired
681 fluorescence spectra, an optical bypass for collected photons was developed using a combination
682 of acousto-optic tunable filters (AOTF, Opto-electronic) (Figure S1). The hyperspectral data were
683 fitted by a suitable spectral model, namely the most convenient empirical log-normal function due
684 to its numerical stability during optimization[69]:

$$I_{\mathrm{LN}}(\lambda) = \begin{cases} \exp\left(-\frac{\log 2}{4a^2}\left[log\left(\frac{4a}{w}(\lambda - \lambda_{\max})\right) + 1\right]^2\right), & \lambda > \lambda_{\max} - \frac{w}{4a} \\ 0, & \lambda \leq \lambda_{\max} - \frac{w}{4a} \end{cases} \quad (2)$$

685

686 with peak position (λ_{max}), approximate full width at half-maximum (FWHM, *w*) and asymmetry (*a*).
687 The developed model was demonstrated to be capable of resolving changes in the spectra as
688 small as 1 nm.[69] Pixel binning of 3x3 was employed prior to spectral fitting, increasing sensitivity
689 at the cost of image resolution.

690 **Scanning electron microscopy with energy-dispersive X-ray spectroscopy (SEM-EDS)**

691 High-resolution imaging and chemical analysis were conducted in the FEI Helios Nanolab 650
692 scanning electron microscope (SEM) utilizing energy-dispersive X-ray spectroscopy (EDS). To
693 prevent the charging effects of a highly insulating biological specimen during electron irradiation,
694 all samples were coated with an approximately 10 nm carbon layer. High-resolution and high
695 surface sensitivity imaging was performed with low electron acceleration voltage (2 keV), low
696 electron current (100 pA) and under high chamber vacuum (10^{-6} hPa). The EDS spectra were
697 collected with higher electron acceleration voltage (15 kV) and electron current (200 pA). Under
698 these conditions, an energy resolution of 145 eV at the Mn Kα line and an elemental sensitivity of
699 approximately 0.01 wt% (X-Max SDD, Oxford Instruments) were achieved. The weight
700 percentage (wt%) of each individual element was calculated and subsequently employed for

701 further analysis, which entailed the measurement of the differences in the wt% ratios of the studied
702 elements between individual regions.

703 **Helium Ion Microsopy (HIM)**

704 High-resolution images at the nanoscale were obtained using a helium ion microscope (Orion
705 NanoFab, Zeiss).[105] For imaging purposes, He atoms are ionized in the GFIS source. The source
706 is characterized by a small virtual source size (0.25mm), a high reduced brightness (1-4 10^9 Am^{-}
707 $^2sr^{-1}V^{-1}$) and a very small energy spread of less than 1 eV. Subsequently the beam is focused,
708 shaped and scanned over the sample surface using electrostatic lenses, quadrupoles, and
709 octapoles. The resulting focused ion beam[106] has a diameter of 0.5 nm and enables the recording
710 of images with a large depth of focus.[107] Prior to imaging, the freeze-dried samples grown on
711 Si_3N_4 substrate were affixed with carbon tape to the standard pins compatible with a multi-pin
712 specimen mount. Insulating samples were spared of conventional thin layer conductive coating
713 due to efficient charge compensation within HIM instrument using the flood gun[108], thus preventing
714 any surface modification at the nanoscale studied. Imaging was conducted through the detection
715 of secondary electrons (SE1) emitted from the few nm surface layer of the sample. The following
716 experimental parameters were employed: helium ion energy (30 keV), ion current (0.5 pA) and
717 chamber vacuum ($2x10^{-7}$ hPa). The field of view (FoV) of the acquired images ranged from less-
718 magnified, 175 μm by 175 μm required for registration, to highly-magnified, 0.7 μm by 0.7 μm,
719 with a minimal pixel step size of 0.7 nm and typical dwell time 20 μs at each pixel.

720 **Synchrotron Micro-X-ray Fluorescence (SR μ-XRF)**

721 The X-ray fluorescence (XRF) data were collected at the TwinMic beamline of Elettra Sincrotrone
722 Trieste, located in Trieste, Italy.[109] The TwinMic microscope was operated in scanning
723 transmission mode, whereby the sample was raster scanned across an incoming perpendicular
724 X-ray beam, delivered by a zone plate diffractive optics. During the scanning process, a rapid
725 readout charge-coupled device (CCD) camera (DV 860, Andor Technology) collected the
726 transmitted X-ray photons, resulting in the generation of absorption and differential phase contrast
727 images.[110] Simultaneously, the emitted X-ray fluorescence (XRF) photons were collected by eight
728 silicon drift detectors (SDD) situated in front of the sample at an angle of 20 degrees with respect
729 to the sample plane.[111] This results in the simultaneous acquisition of both, the morphology of the
730 sample and the distribution of the elements.

731 In order to achieve optimal excitation of Mg, Na, O, Ti and C, while also obtaining sub-micron
732 spatial resolution, a monochromatic energy of 1.5 keV was selected for the experiment. The

specimens were scanned at a step size of 500 nm with a probe size of 600 nm in diameter, delivered by an Au zone plate of 600 μm diameter and 50 nm outermost zone width. An acquisition time of 50 ms pixel^{-1} and 4 s pixel^{-1} were employed for the CCD and SDD detector systems, respectively. The acquired XRF spectra were processed using the PyMCA software.[112]

Supporting Information

Additional high resolution and correlative microscopy results of the nano-bio interface supporting the investigated possible modes of action leading to nanoparticle induced lung epithelial toxicity.

Acknowledgements

This work was supported by Helmholtz European Partnering project CROSSING (Grant No: PIE-0007), EU H2020 project no. 824096 “RADIATE”, the Slovenian research and innovation agency (ARIS) programs P1-0060 (Experimental biophysics of complex systems), P1-0112, I0-0005 and project N1-0090. The authors thank Prof. Dr. Katarina Vogel Mikuš of the Biotechnical Faculty (University of Ljubljana) for her invaluable assistance with the freeze-drying of samples, Dr. Valentina Bonanni of the Elettra Sincrotrone (Trieste, Italy) for help with the SR μXRF measurements, Prof. Dr. Janez Štrancar of the Jožef Stefan Institute (Ljubljana, Slovenia) for initiating the scientific field in the Laboratory of Biophysics, Dr. Tilen Koklič for fruitful discussions, Dr. Iztok Urbančič for the hyperspectral analysis software support, DR. Stane Pajk for the synthesis of lipid droplet dye, Dr. Polona Umek for synthesis of TiO_2 nanoparticles and Dr. Hana Kokot for fluorescence labeling of TiO_2 nanoparticles (all of the Jožef Stefan Institute).

Author contributions

R.P. conceptualized and designed the analysis; R.P., A.K., L.P. and A.G. performed the experiments; R.P., L.H. and A.G. collected the data; R.P. performed the analysis and data visualization; R.P., G.H. and A.G. contributed analysis tools; R.P. wrote the paper; R.P., L.P., G.H., A.G. and P.P. reviewed and edited the paper; P.P. acquired funding.

References

(1) Correlative Light and Electron Microscopy IV, Volume 162 - 1st Edition, In *Methods in Cell Biology,* Reichert, T. M.; Verkade, P., Eds.; Academic Press, 2021; pp 2-430.
(2) Ando, T.; Bhamidimarri, S. P.; Brending, N.; Colin-York, H.; Collinson, L.; Jonge, N. D.; Pablo, P. J. de; Debroye, E.; Eggeling, C.; Franck, C.; Fritzsche, M.; Gerritsen, H.; Giepmans, B. N. G.; Grunewald, K.; Hofkens, J.; Hoogenboom, J. P.; Janssen, K. P. F.; Kaufmann, R.; Klumperman, J.; Kurniawan, N., et al. The 2018 Correlative Microscopy Techniques Roadmap. *J. Phys. D: Appl. Phys.* **2018**, *51* (44), 443001.
(3) Datta, R.; Heaster, T. M.; Sharick, J. T.; Gillette, A. A.; Skala, M. C. Fluorescence Lifetime Imaging Microscopy: Fundamentals and Advances in Instrumentation, Analysis, and Applications. *J Biomed Opt* **2020**, *25* (7), 1–43.
(4) Sekar, R. B.; Periasamy, A. Fluorescence Resonance Energy Transfer (FRET) Microscopy Imaging of Live Cell Protein Localizations. *J Cell Biol* **2003**, *160* (5), 629–633.
(5) Varsano, N.; Wolf, S. G. Electron Microscopy of Cellular Ultrastructure in Three Dimensions. *Current Opinion in Structural Biology* **2022**, *76*, 102444.
(6) Nuñez, J.; Renslow, R.; Cliff, J. B.; Anderton, C. R. NanoSIMS for Biological Applications: Current Practices and Analyses. *Biointerphases* **2017**, *13* (3), 03B301.
(7) De Samber, B.; De Rycke, R.; De Bruyne, M.; Kienhuis, M.; Sandblad, L.; Bohic, S.; Cloetens, P.; Urban, C.; Polerecky, L.; Vincze, L. Effect of Sample Preparation Techniques upon Single Cell Chemical Imaging: A Practical Comparison between Synchrotron Radiation Based X-Ray Fluorescence (SR-XRF) and Nanoscopic Secondary Ion Mass Spectrometry (Nano-SIMS). *Anal Chim Acta* **2020**, *1106*, 22–32.
(8) Manisalidis, I.; Stavropoulou, E.; Stavropoulos, A.; Bezirtzoglou, E. Environmental and Health Impacts of Air Pollution: A Review. *Front Public Health* **2020**, *8*, 14.
(9) Moreno-Ríos, A. L.; Tejeda-Benítez, L. P.; Bustillo-Lecompte, C. F. Sources, Characteristics, Toxicity, and Control of Ultrafine Particles: An Overview. *Geoscience Frontiers* **2022**, *13* (1), 101147.
(10) Hill, W.; Lim, E. L.; Weeden, C. E.; Lee, C.; Augustine, M.; Chen, K.; Kuan, F.-C.; Marongiu, F.; Evans, E. J.; Moore, D. A.; Rodrigues, F. S.; Pich, O.; Bakker, B.; Cha, H.; Myers, R.; van Maldegem, F.; Boumelha, J.; Veeriah, S.; Rowan, A.; Naceur-Lombardelli, C., et al. Lung Adenocarcinoma Promotion by Air Pollutants. *Nature* **2023**, *616* (7955), 159–167.
(11) You, D. J.; Bonner, J. C. Susceptibility Factors in Chronic Lung Inflammatory Responses to Engineered Nanomaterials. *Int J Mol Sci* **2020**, *21* (19), 7310.
(12) Kempen, P. J.; Kircher, M. F.; de la Zerda, A.; Zavaleta, C. L.; Jokerst, J. V.; Mellinghoff, I. K.; Gambhir, S. S.; Sinclair, R. A Correlative Optical Microscopy and Scanning Electron Microscopy Approach to Locating Nanoparticles in Brain Tumors. *Micron* **2015**, *68*, 70–76.
(13) Han, S.; Raabe, M.; Hodgson, L.; Mantell, J.; Verkade, P.; Lasser, T.; Landfester, K.; Weil, T.; Lieberwirth, I. High-Contrast Imaging of Nanodiamonds in Cells by Energy Filtered and Correlative Light-Electron Microscopy: Toward a Quantitative Nanoparticle-Cell Analysis. *Nano Lett.* **2019**, *19* (3), 2178–2185.
(14) Hayashi, Y.; Takamiya, M.; Jensen, P. B.; Ojea-Jiménez, I.; Claude, H.; Antony, C.; Kjaer-Sorensen, K.; Grabher, C.; Boesen, T.; Gilliland, D.; Oxvig, C.; Strähle, U.; Weiss, C. Differential Nanoparticle Sequestration by Macrophages and Scavenger Endothelial

Cells Visualized in Vivo in Real-Time and at Ultrastructural Resolution. *ACS Nano* **2020**, *14* (2), 1665–1681.

(15) García-Serradilla, M.; Risco, C. Light and Electron Microscopy Imaging Unveils New Aspects of the Antiviral Capacity of Silver Nanoparticles in Bunyavirus-Infected Cells. *Virus Research* **2021**, *302*, 198444.

(16) Kopek, B. G.; Paez-Segala, M. G.; Shtengel, G.; Sochacki, K. A.; Sun, M. G.; Wang, Y.; Xu, C. S.; van Engelenburg, S. B.; Taraska, J. W.; Looger, L. L.; Hess, H. F. Diverse Protocols for Correlative Super-Resolution Fluorescence Imaging and Electron Microscopy of Chemically Fixed Samples. *Nat Protoc* **2017**, *12* (5), 916–946.

(17) Gallagher-Jones, M.; Dias, C. S. B.; Pryor, A.; Bouchmella, K.; Zhao, L.; Lo, Y. H.; Cardoso, M. B.; Shapiro, D.; Rodriguez, J.; Miao, J. Correlative Cellular Ptychography with Functionalized Nanoparticles at the Fe L-Edge. *Sci Rep* **2017**, *7*, 4757.

(18) Liu, M.; Li, Q.; Liang, L.; Li, J.; Wang, K.; Li, J.; Lv, M.; Chen, N.; Song, H.; Lee, J.; Shi, J.; Wang, L.; Lal, R.; Fan, C. Real-Time Visualization of Clustering and Intracellular Transport of Gold Nanoparticles by Correlative Imaging. *Nat Commun* **2017**, *8* (1), 15646.

(19) Bhat, S. V.; Sultana, T.; Körnig, A.; McGrath, S.; Shahina, Z.; Dahms, T. E. S. Correlative Atomic Force Microscopy Quantitative Imaging-Laser Scanning Confocal Microscopy Quantifies the Impact of Stressors on Live Cells in Real-Time. *Sci Rep* **2018**, *8* (1), 8305.

(20) Lo Giudice, C.; Yang, J.; Poncin, M. A.; Adumeau, L.; Delguste, M.; Koehler, M.; Evers, K.; Dumitru, A. C.; Dawson, K. A.; Alsteens, D. Nanophysical Mapping of Inflammasome Activation by Nanoparticles via Specific Cell Surface Recognition Events. *ACS Nano* **2022**, *16* (1), 306–316.

(21) Mi, Z.; Chen, C.-B.; Tan, H. Q.; Dou, Y.; Yang, C.; Turaga, S. P.; Ren, M.; Vajandar, S. K.; Yuen, G. H.; Osipowicz, T.; Watt, F.; Bettiol, A. A. Quantifying Nanodiamonds Biodistribution in Whole Cells with Correlative Iono-Nanoscopy. *Nat Commun* **2021**, *12* (1), 4657.

(22) Le Trequesser, Q.; Devès, G.; Saez, G.; Daudin, L.; Barberet, P.; Michelet, C.; Delville, M.-H.; Seznec, H. Single Cell In Situ Detection and Quantification of Metal Oxide Nanoparticles Using Multimodal Correlative Microscopy. *Anal. Chem.* **2014**, *86* (15), 7311–7319.

(23) Podlipec, R.; Punzón-Quijorna, E.; Pirker, L.; Kelemen, M.; Vavpetič, P.; Kavalar, R.; Hlawacek, G.; Štrancar, J.; Pelicon, P.; Fokter, S. K. Revealing Inflammatory Indications Induced by Titanium Alloy Wear Debris in Periprosthetic Tissue by Label-Free Correlative High-Resolution Ion, Electron and Optical Microspectroscopy. *Materials* **2021**, *14* (11), 3048.

(24) Quintana, C.; Wu, T.-D.; Delatour, B.; Dhenain, M.; Guerquin-Kern, J. luc; Croisy, A. Morphological and Chemical Studies of Pathological Human and Mice Brain at the Subcellular Level: Correlation between Light, Electron, and Nanosims Microscopies. *Microscopy Research and Technique* **2007**, *70* (4), 281–295.

(25) Audinot, J.-N.; Georgantzopoulou, A.; Piret, J.-P.; Gutleb, A. C.; Dowsett, D.; Migeon, H. N.; Hoffmann, L. Identification and Localization of Nanoparticles in Tissues by Mass Spectrometry. *Surface and Interface Analysis* **2013**, *45* (1), 230–233.

(26) Vollnhals, F.; Audinot, J.-N.; Wirtz, T.; Mercier-Bonin, M.; Fourquaux, I.; Schroeppel, B.; Kraushaar, U.; Lev-Ram, V.; Ellisman, M. H.; Eswara, S. Correlative Microscopy Combining Secondary Ion Mass Spectrometry and Electron Microscopy: Comparison of

Intensity–Hue–Saturation and Laplacian Pyramid Methods for Image Fusion. *Anal. Chem.* **2017**, *89* (20), 10702–10710.

(27) Lovric, J.; Audinot, J.-N.; Wirtz, T. In Situ Correlative Helium Ion Microscopy and Secondary Ion Mass Spectrometry for High-Resolution Nano-Analytics in Life Sciences. *Microscopy and Microanalysis* **2019**, *25* (S2), 1026–1027.

(28) Biesemeier, A.; Castro, O. D.; Serralta, E.; Lovric, J.; Eswara, S.; Audinot, J.-N.; Cambier, S.; Wirtz, T. Correlative Electron Microscopy, High Resolution Ion Imaging and Secondary Ion Mass Spectrometry for High Resolution Nanoanalytics on Biological Tissue. *Microscopy and Microanalysis* **2020**, *26* (S2), 818–820.

(29) De Castro, O.; Biesemeier, A.; Serralta, E.; Bouton, O.; Barrahma, R.; Hoang, Q. H.; Cambier, S.; Taubitz, T.; Klingner, N.; Hlawacek, G.; Pinto, S. D.; Gnauck, P.; Lucas, F.; Bebeacua, C.; Wirtz, T. npSCOPE: A New Multimodal Instrument for In Situ Correlative Analysis of Nanoparticles. *Anal. Chem.* **2021**, *93* (43), 14417–14424.

(30) Le Trequesser, Q.; Saez, G.; Simon, M.; Devès, G.; Daudin, L.; Barberet, P.; Michelet, C.; Delville, M.-H.; Seznec, H. Multimodal Correlative Microscopy for in Situ Detection and Quantification of Chemical Elements in Biological Specimens. Applications to Nanotoxicology. *J Chem Biol* **2015**, *8* (4), 159–167.

(31) James, S. A.; Feltis, B. N.; de Jonge, M. D.; Sridhar, M.; Kimpton, J. A.; Altissimo, M.; Mayo, S.; Zheng, C.; Hastings, A.; Howard, D. L.; Paterson, D. J.; Wright, P. F. A.; Moorhead, G. F.; Turney, T. W.; Fu, J. Quantification of ZnO Nanoparticle Uptake, Distribution, and Dissolution within Individual Human Macrophages. *ACS Nano* **2013**, *7* (12), 10621–10635.

(32) Tardillo Suárez, V.; Gallet, B.; Chevallet, M.; Jouneau, P.-H.; Tucoulou, R.; Veronesi, G.; Deniaud, A. Correlative Transmission Electron Microscopy and High-Resolution Hard X-Ray Fluorescence Microscopy of Cell Sections to Measure Trace Element Concentrations at the Organelle Level. *Journal of Structural Biology* **2021**, *213* (3), 107766.

(33) Malucelli, E.; Iotti, S.; Gianoncelli, A.; Fratini, M.; Merolle, L.; Notargiacomo, A.; Marraccini, C.; Sargenti, A.; Cappadone, C.; Farruggia, G.; Bukreeva, I.; Lombardo, M.; Trombini, C.; Maier, J. A.; Lagomarsino, S. Quantitative Chemical Imaging of the Intracellular Spatial Distribution of Fundamental Elements and Light Metals in Single Cells. *Anal Chem* **2014**, *86* (10), 5108–5115.

(34) Perrin, L.; Carmona, A.; Roudeau, S.; Ortega, R. Evaluation of Sample Preparation Methods for Single Cell Quantitative Elemental Imaging Using Proton or Synchrotron Radiation Focused Beams. *J. Anal. At. Spectrom.* **2015**, *30* (12), 2525–2532.

(35) Jobim, P. F. C.; Iochims dos Santos, C. E.; Dias, J. F.; Kelemen, M.; Pelicon, P.; Mikuš, K. V.; Pascolo, L.; Gianoncelli, A.; Bedolla, D. E.; Rasia-Filho, A. A. Human Neocortex Layer Features Evaluated by PIXE, STIM, and STXM Techniques. *Biol Trace Elem Res* **2023**, *201* (2), 592–602.

(36) Pongrac, P.; Vogel-Mikuš, K.; Jeromel, L.; Vavpetič, P.; Pelicon, P.; Kaulich, B.; Gianoncelli, A.; Eichert, D.; Regvar, M.; Kreft, I. Spatially Resolved Distributions of the Mineral Elements in the Grain of Tartary Buckwheat (*Fagopyrum Tataricum*). *Food Research International* **2013**, *54* (1), 125–131.

(37) Bischof, J.; Fletcher, G.; Verkade, P.; Kuntner, C.; Fernandez-Rodriguez, J.; Chaabane, L.; Rose, L. A.; Walter, A.; Vandenbosch, M.; van Zandvoort, M. A. M. J.; Zaritsky, A.; Keppler, A.; Parsons, M. Multimodal Bioimaging across Disciplines and Scales: Challenges, Opportunities and Breaking down Barriers. *npj Imaging* **2024**, *2* (1), 1–6.

(38) Oberdörster, G.; Maynard, A.; Donaldson, K.; Castranova, V.; Fitzpatrick, J.; Ausman, K.; Carter, J.; Karn, B.; Kreyling, W.; Lai, D.; Olin, S.; Monteiro-Riviere, N.; Warheit, D.; Yang, H.; A report from the ILSI Research Foundation/Risk Science Institute Nanomaterial Toxicity Screening Working Group. Principles for Characterizing the Potential Human Health Effects from Exposure to Nanomaterials: Elements of a Screening Strategy. *Particle and Fibre Toxicology* **2005**, *2* (1), 8.

(39) Kokot, H.; Kokot, B.; Sebastijanović, A.; Voss, C.; Podlipec, R.; Zawilska, P.; Berthing, T.; Ballester-López, C.; Danielsen, P. H.; Contini, C.; Ivanov, M.; Krišelj, A.; Čotar, P.; Zhou, Q.; Ponti, J.; Zhernovkov, V.; Schneemilch, M.; Doumandji, Z.; Pušnik, M.; Umek, P.; Pajk, S., et al., J. Prediction of Chronic Inflammation for Inhaled Particles: The Impact of Material Cycling and Quarantining in the Lung Epithelium. *Advanced Materials* **2020**, *32* (47), 2003913.

(40) Danielsen, P. H.; Knudsen, K. B.; Štrancar, J.; Umek, P.; Koklič, T.; Garvas, M.; Vanhala, E.; Savukoski, S.; Ding, Y.; Madsen, A. M.; Jacobsen, N. R.; Weydahl, I. K.; Berthing, T.; Poulsen, S. S.; Schmid, O.; Wolff, H.; Vogel, U. Effects of Physicochemical Properties of TiO2 Nanomaterials for Pulmonary Inflammation, Acute Phase Response and Alveolar Proteinosis in Intratracheally Exposed Mice. *Toxicology and Applied Pharmacology* **2020**, *386*, 114830.

(41) Podlipec, R.; Sebastijanovič, A.; Cassidy, H.; Han, L.; Danielsen, P.; Čotar, P.; Kokot, H.; Koser, B. K.; Vencelj, A.; Pirker, L.; Umek, P.; Hlawacek, G.; Heller, R.; Matallanas, D.; Pelicon, P.; Stoeger, T.; Urbančič, I.; Vogel, U.; Koklič, T.; Štrancar, J. Binucleated Cell Formation and Oncogene Expression after Particulate Matter Exposure Is Preceded by Microtubule Disruption, Dysregulated Cell Cycle, Prolonged Mitosis, and Septin Binding. bioRxiv, https://doi.org/10.1101/2024.01.07.574515.

(42) Zhang, Y.; Huang, T.; Jorgens, D. M.; Nickerson, A.; Lin, L.-J.; Pelz, J.; Gray, J. W.; López, C. S.; Nan, X. Quantitating Morphological Changes in Biological Samples during Scanning Electron Microscopy Sample Preparation with Correlative Super-Resolution Microscopy. *PLoS One* **2017**, *12* (5), e0176839.

(43) Li, Y.; Almassalha, L. M.; Chandler, J. E.; Zhou, X.; Stypula-Cyrus, Y. E.; Hujsak, K. A.; Roth, E. W.; Bleher, R.; Subramanian, H.; Szleifer, I.; Dravid, V. P.; Backman, V. The Effects of Chemical Fixation on the Cellular Nanostructure. *Exp Cell Res* **2017**, *358* (2), 253–259.

(44) Murk, J. L. a. N.; Posthuma, G.; Koster, A. J.; Geuze, H. J.; Verkleij, A. J.; Kleijmeer, M. J.; Humbel, B. M. Influence of Aldehyde Fixation on the Morphology of Endosomes and Lysosomes: Quantitative Analysis and Electron Tomography. *Journal of Microscopy* **2003**, *212* (1), 81–90.

(45) Ebersold, H. R.; Cordier, J. L.; Lüthy, P. Bacterial Mesosomes: Method Dependent Artifacts. *Arch Microbiol* **1981**, *130* (1), 19–22.

(46) Idziak, A.; Inavalli, V. V. G. K.; Bancelin, S.; Arizono, M.; Nägerl, U. V. The Impact of Chemical Fixation on the Microanatomy of Mouse Organotypic Hippocampal Slices. *eNeuro* **2023**, *10* (9).

(47) Parlanti, P.; Cappello, V. Microscopes, Tools, Probes, and Protocols: A Guide in the Route of Correlative Microscopy for Biomedical Investigation. *Micron* **2022**, *152*, 103182.

(48) Kokot, B.; Kokot, H.; Umek, P.; van Midden, K. P.; Pajk, S.; Garvas, M.; Eggeling, C.; Koklič, T.; Urbančič, I.; Štrancar, J. How to Control Fluorescent Labeling of Metal Oxide

Nanoparticles for Artefact-Free Live Cell Microscopy. *Nanotoxicology* **2021**, *15* (8), 1102–1123.

44. Suhling, K. *et al.* Fluorescence Lifetime Imaging. in *Handbook of Photonics for Biomedical Engineering* (eds. Ho, A. H.-P., Kim, D. & Somekh, M. G.) 1–50 (Springer Netherlands, Dordrecht, 2021).

(50) Strickfaden, H. Reflections on the Organization and the Physical State of Chromatin in Eukaryotic Cells. *Genome* **2021**, *64* (4), 311–325.

(51) Shrestha, D.; Jenei, A.; Nagy, P.; Vereb, G.; Szöllősi, J. Understanding FRET as a Research Tool for Cellular Studies. *Int J Mol Sci* **2015**, *16* (4), 6718–6756.

(52) Miller, K. N.; Victorelli, S. G.; Salmonowicz, H.; Dasgupta, N.; Liu, T.; Passos, J. F.; Adams, P. D. Cytoplasmic DNA: Sources, Sensing, and Role in Aging and Disease. *Cell* **2021**, *184* (22), 5506–5526.

(53) Pol, E. van der; Böing, A. N.; Harrison, P.; Sturk, A.; Nieuwland, R. Classification, Functions, and Clinical Relevance of Extracellular Vesicles. *Pharmacol Rev* **2012**, *64* (3), 676–705.

(54) Goldstein, J. I.; Newbury, D. E.; Michael, J. R.; Ritchie, N. W. M.; Scott, J. H. J.; Joy, D. C. Energy Dispersive X-Ray Spectrometry: Physical Principles and User-Selected Parameters. In *Scanning Electron Microscopy and X-Ray Microanalysis*; Goldstein, J. I., Newbury, D. E., Michael, J. R., Ritchie, N. W. M., Scott, J. H. J., Joy, D. C., Eds.; Springer: New York, NY, 2018; pp 209–234.

(55) Urbančič, I.; Garvas, M.; Kokot, B.; Majaron, H.; Umek, P.; Cassidy, H.; Škarabot, M.; Schneider, F.; Galiani, S.; Arsov, Z.; Koklic, T.; Matallanas, D.; Čeh, M.; Muševič, I.; Eggeling, C.; Štrancar, J. Nanoparticles Can Wrap Epithelial Cell Membranes and Relocate Them Across the Epithelial Cell Layer. *Nano Lett.* **2018**, *18* (8), 5294–5305.

(56) Elzanowska, J.; Semira, C.; Costa-Silva, B. DNA in Extracellular Vesicles: Biological and Clinical Aspects. *Molecular Oncology* **2020**, *15* (6), 1701.

(57) Wyllie, A. H.; Kerr, J. F.; Currie, A. R. Cell Death: The Significance of Apoptosis. *Int Rev Cytol* **1980**, *68*, 251–306.

(58) Karbowski, M.; Youle, J. R., Dynamics of mitochondrial morphology in healthy cells and during apoptosis*, Cell Death Differ.* **2003**, *10*, 870-880.

(59) Zhang, X.; Wang, F.; Liu, B.; Kelly, E. Y.; Servos, M. R.; Liu, J. Adsorption of DNA Oligonucleotides by Titanium Dioxide Nanoparticles. *Langmuir* **2014**, *30* (3), 839–845.

(60) Bischoff, M.; Biriukov, D.; Předota, M.; Roke, S.; Marchioro, A. Surface Potential and Interfacial Water Order at the Amorphous TiO2 Nanoparticle/Aqueous Interface. *J. Phys. Chem. C* **2020**, *124* (20), 10961–10974.

(61) Shukla, R. K.; Badiye, A.; Vajpayee, K.; Kapoor, N. Genotoxic Potential of Nanoparticles: Structural and Functional Modifications in DNA. *Front Genet* **2021**, *12*, 728250.

(62) Morrow, P. Possible Mechanisms to Explain Dust Overloading of the Lungs. *Fundamental and Applied Toxicology* **1988**, *10* (3), 369–384.

(63) Sachet, M.; Liang, Y. Y.; Oehler, R. The Immune Response to Secondary Necrotic Cells. *Apoptosis* **2017**, *22* (10), 1189–1204.

(64) Degen, M.; Santos, J. C.; Pluhackova, K.; Cebrero, G.; Ramos, S.; Jankevicius, G.; Hartenian, E.; Guillerm, U.; Mari, S. A.; Kohl, B.; Müller, D. J.; Schanda, P.; Maier, T.; Perez, C.; Sieben, C.; Broz, P.; Hiller, S. Structural Basis of NINJ1-Mediated Plasma Membrane Rupture in Cell Death. *Nature* **2023**, *618* (7967), 1065–1071.

(65) Zhao, C.; Pu, W.; Niu, M.; Wazir, J.; Song, S.; Wei, L.; Li, L.; Su, Z.; Wang, H. Respiratory Exposure to PM2.5 Soluble Extract Induced Chronic Lung Injury by Disturbing the Phagocytosis Function of Macrophage. *Environ Sci Pollut Res* **2022**, *29* (10), 13983–13997.
(66) Gustafson, H. H.; Holt-Casper, D.; Grainger, D. W.; Ghandehari, H. Nanoparticle Uptake: The Phagocyte Problem. *Nano Today* **2015**, *10* (4), 487–510.
(67) Chen, Q.; Wang, N.; Zhu, M.; Lu, J.; Zhong, H.; Xue, X.; Guo, S.; Li, M.; Wei, X.; Tao, Y.; Yin, H. TiO2 Nanoparticles Cause Mitochondrial Dysfunction, Activate Inflammatory Responses, and Attenuate Phagocytosis in Macrophages: A Proteomic and Metabolomic Insight. *Redox Biology* **2018**, *15*, 266–276.
(68) Gianoncelli, A.; Bonanni, V.; Gariani, G.; Guzzi, F.; Pascolo, L.; Borghes, R.; Billè, F.; Kourousias, G. Soft X-Ray Microscopy Techniques for Medical and Biological Imaging at TwinMic—Elettra. *Applied Sciences* **2021**, *11* (16), 7216.
(69) Urbančič, I.; Arsov, Z.; Ljubetič, A.; Biglino, D.; Strancar, J. Bleaching-Corrected Fluorescence Microspectroscopy with Nanometer Peak Position Resolution. *Opt Express* **2013**, *21* (21), 25291–25306.
53. Solvent and Environmental Effects. in *Principles of Fluorescence Spectroscopy* (ed. Lakowicz, J. R.) 205–235 (Springer US, Boston, MA, 2006).
(71) Berman, E. S. F.; Fortson, S. L.; Checchi, K. D.; Wu, L.; Felton, J. S.; Wu, K. J. J.; Kulp, K. S. Preparation of Single Cells for Imaging/Profiling Mass Spectrometry. *Journal of the American Society for Mass Spectrometry* **2008**, *19* (8), 1230–1236.
(72) Liu, Y.; Tan, J.; Thomas, A.; Ou-Yang, D.; Muzykantov, V. R. The Shape of Things to Come: Importance of Design in Nanotechnology for Drug Delivery. *Ther Deliv* **2012**, *3* (2), 181–194.
(73) Lesniak, A.; Fenaroli, F.; Monopoli, M. P.; Åberg, C.; Dawson, K. A.; Salvati, A. Effects of the Presence or Absence of a Protein Corona on Silica Nanoparticle Uptake and Impact on Cells. *ACS Nano* **2012**, *6* (7), 5845–5857.
(74) First-Principles Study of Na Insertion at TiO2 Anatase Surfaces: New Hints for Na-Ion Battery Design. *Nanoscale Advances* **2020**, *2* (7), 2745–2751.
(75) Shriver, Z.; Capila, I.; Venkataraman, G.; Sasisekharan, R. Heparin and Heparan Sulfate: Analyzing Structure and Microheterogeneity. *Handb Exp Pharmacol* **2012**, No. 207, 159–176.
(76) Farrugia, B. L.; Lord, M. S.; Melrose, J.; Whitelock, J. M. The Role of Heparan Sulfate in Inflammation, and the Development of Biomimetics as Anti-Inflammatory Strategies. *J Histochem Cytochem* **2018**, *66* (4), 321–336.
(77) Lu, M.; Kaminski, C. F.; Schierle, G. S. K. Advanced Fluorescence Imaging of in Situ Protein Aggregation. *Phys Biol* **2020**, *17* (2), 021001.
(78) Rustom, A.; Saffrich, R.; Markovic, I.; Walther, P.; Gerdes, H.-H. Nanotubular Highways for Intercellular Organelle Transport. *Science* **2004**, *303* (5660), 1007–1010.
(79) Donovan, A.; Lima, C. A.; Pinkus, J. L.; Pinkus, G. S.; Zon, L. I.; Robine, S.; Andrews, N. C. The Iron Exporter Ferroportin/Slc40a1 Is Essential for Iron Homeostasis. *Cell Metabolism* **2005**, *1* (3), 191–200.
(80) Nakamura, T.; Naguro, I.; Ichijo, H. Iron Homeostasis and Iron-Regulated ROS in Cell Death, Senescence and Human Diseases. *Biochimica et Biophysica Acta (BBA) - General Subjects* **2019**, *1863* (9), 1398–1409.

(81) Nano, G. V.; Strathmann, T. J. Ferrous Iron Sorption by Hydrous Metal Oxides. *Journal of Colloid and Interface Science* **2006**, *297* (2), 443–454.
(82) Mayer, K. M.; Hafner, J. H. Localized Surface Plasmon Resonance Sensors. *Chem. Rev.* **2011**, *111* (6), 3828–3857.
(83) Tang, L.; Casas, J.; Venkataramasubramani, M. Magnetic Nanoparticle Mediated Enhancement of Localized Surface Plasmon Resonance for Ultrasensitive Bioanalytical Assay in Human Blood Plasma. *Anal Chem* **2013**, *85* (3), 1431–1439.
(84) Li, J.; Krasavin, A. V.; Webster, L.; Segovia, P.; Zayats, A. V.; Richards, D. Spectral Variation of Fluorescence Lifetime near Single Metal Nanoparticles. *Sci Rep* **2016**, *6* (1), 21349.
(85) Li, J.; Cao, F.; Yin, H.; Huang, Z.; Lin, Z.; Mao, N.; Sun, B.; Wang, G. Ferroptosis: Past, Present and Future. *Cell Death Dis* **2020**, *11* (2), 1–13.
(86) Danylchuk, D. I.; Jouard, P.-H.; Klymchenko, A. S. Targeted Solvatochromic Fluorescent Probes for Imaging Lipid Order in Organelles under Oxidative and Mechanical Stress. *J Am Chem Soc* **2021**, *143* (2), 912–924.
(87) Ryan, E.; Mockros, L.; Weisel, J.; Lorand, L. Structural Origins of Fibrin Clot Rheology. *Biophys J* **1999**, *77* (5), 2813–2826.
(88) Li, W.; Sigley, J.; Pieters, M.; Helms, C. C.; Nagaswami, C.; Weisel, J. W.; Guthold, M. Fibrin Fiber Stiffness Is Strongly Affected by Fiber Diameter, but Not by Fibrinogen Glycation. *Biophys J* **2016**, *110* (6), 1400–1410.
(89) Idell, S.; James, K. K.; Levin, E. G.; Schwartz, B. S.; Manchanda, N.; Maunder, R. J.; Martin, T. R.; McLarty, J.; Fair, D. S. Local Abnormalities in Coagulation and Fibrinolytic Pathways Predispose to Alveolar Fibrin Deposition in the Adult Respiratory Distress Syndrome. *J Clin Invest* **1989**, *84* (2), 695–705.
(90) Idell, S. Coagulation, Fibrinolysis, and Fibrin Deposition in Acute Lung Injury. *Crit Care Med* **2003**, *31* (4 Suppl), S213-220.
(91) Guadiz, G.; Sporn, L. A.; Goss, R. A.; Lawrence, S. O.; Marder, V. J.; Simpson-Haidaris, P. J. Polarized Secretion of Fibrinogen by Lung Epithelial Cells. *Am J Respir Cell Mol Biol* **1997**, *17* (1), 60–69.
(92) Bastarache, J. A.; Sebag, S. C.; Grove, B. S.; Ware, L. B. IFN-γ and TNF-α Act Synergistically to Upregulate Tissue Factor in Alveolar Epithelial Cells. *Exp Lung Res* **2011**, *37* (8), 509–517.
(93) Naji, A.; Muzembo, B. A.; Yagyu, K.; Baba, N.; Deschaseaux, F.; Sensebé, L.; Suganuma, N. Endocytosis of Indium-Tin-Oxide Nanoparticles by Macrophages Provokes Pyroptosis Requiring NLRP3-ASC-Caspase1 Axis That Can Be Prevented by Mesenchymal Stem Cells. *Sci Rep* **2016**, *6* (1), 26162.
(94) Erdem, J. S.; Závodná, T.; Ervik, T. K.; Skare, Ø.; Hron, T.; Anmarkrud, K. H.; Kuśnierczyk, A.; Catalán, J.; Ellingsen, D. G.; Topinka, J.; Zienolddiny-Narui, S. High Aspect Ratio Nanomaterial-Induced Macrophage Polarization Is Mediated by Changes in miRNA Levels. *Front Immunol* **2023**, *14*, 1111123.
(95) Garvas, M.; Testen, A.; Umek, P.; Gloter, A.; Koklic, T.; Strancar, J. Protein Corona Prevents TiO2 Phototoxicity. *PLoS One* **2015**, *10* (6), e0129577.
(96) Baranowska-Wójcik, E.; Szwajgier, D.; Oleszczuk, P.; Winiarska-Mieczan, A. Effects of Titanium Dioxide Nanoparticles Exposure on Human Health—a Review. *Biol Trace Elem Res* **2020**, *193* (1), 118–129.

(97) Gutierrez, C. T.; Loizides, C.; Hafez, I.; Brostrøm, A.; Wolff, H.; Szarek, J.; Berthing, T.; Mortensen, A.; Jensen, K. A.; Roursgaard, M.; Saber, A. T.; Møller, P.; Biskos, G.; Vogel, U. Acute Phase Response Following Pulmonary Exposure to Soluble and Insoluble Metal Oxide Nanomaterials in Mice. *Particle and Fibre Toxicology* **2023**, *20* (1), 4.
(98) Wang, J. J.; Sanderson, B. J. S.; Wang, H. Cyto- and Genotoxicity of Ultrafine TiO2 Particles in Cultured Human Lymphoblastoid Cells. *Mutation Research/Genetic Toxicology and Environmental Mutagenesis* **2007**, *628* (2), 99–106.
(99) Schmid, O.; Stoeger, T. Surface Area Is the Biologically Most Effective Dose Metric for Acute Nanoparticle Toxicity in the Lung. *Journal of Aerosol Science* **2016**, *99*, 133–143.
(100) Jackson, P.; Halappanavar, S.; Hougaard, K. S.; Williams, A.; Madsen, A. M.; Lamson, J. S.; Andersen, O.; Yauk, C.; Wallin, H.; Vogel, U. Maternal Inhalation of Surface-Coated Nanosized Titanium Dioxide (UV-Titan) in C57BL/6 Mice: Effects in Prenatally Exposed Offspring on Hepatic DNA Damage and Gene Expression. *Nanotoxicology* **2013**, *7* (1), 85–96.
(101) Tivol, W. F.; Briegel, A.; Jensen, G. J. An Improved Cryogen for Plunge Freezing. *Microsc Microanal* **2008**, *14* (5), 375–379.
(102) Becker, W. *The Bh TCSPC Handbook 10th Edition, 2023*.
(103) Podlipec, R.; Mur, J.; Petelin, J.; Štrancar, J.; Petkovšek, R. Two-Photon Retinal Theranostics by Adaptive Compact Laser Source. *Appl. Phys. A* **2020**, *126* (6), 405.
(104) Podlipec, R.; Mur, J.; Petelin, J.; Štrancar, J.; Petkovšek, R. Method for Controlled Tissue Theranostics Using a Single Tunable Laser Source. *Biomed Opt Express* **2021**, *12* (9), 5881–5893.
(105) *Helium Ion Microscopy*; Hlawacek, G., Gölzhäuser, A., Eds.; NanoScience and Technology; Springer International Publishing: Cham, 2016.
(106) Höflich, K.; Hobler, G.; Allen, F. I.; Wirtz, T.; Rius, G.; McElwee-White, L.; Krasheninnikov, A. V.; Schmidt, M.; Utke, I.; Klingner, N.; Osenberg, M.; Córdoba, R.; Djurabekova, F.; Manke, I.; Moll, P.; Manoccio, M.; De Teresa, J. M.; Bischoff, L.; Michler, J.; De Castro, O., et al. Roadmap for Focused Ion Beam Technologies. *Applied Physics Reviews* **2023**, *10* (4), 041311.
(107) Hlawacek, G.; Veligura, V.; van Gastel, R.; Poelsema, B. Helium Ion Microscopy. *Journal of Vacuum Science & Technology B* **2014**, *32* (2), 020801. https://doi.org/10.1116/1.4863676.
(108) Schmidt, M.; Byrne, J. M.; Maasilta, I. J. Bio-Imaging with the Helium-Ion Microscope: A Review. *Beilstein J. Nanotechnol.* **2021**, *12* (1), 1–23.
(109) Gianoncelli, A.; Kourousias, G.; Merolle, L.; Altissimo, M.; Bianco, A. Current Status of the TwinMic Beamline at Elettra: A Soft X-Ray Transmission and Emission Microscopy Station. *J Synchrotron Radiat* **2016**, *23* (Pt 6), 1526–1537.
(110) Gianoncelli, A.; Morrison, G. R.; Kaulich, B.; Bacescu, D.; Kovac, J. Scanning Transmission X-Ray Microscopy with a Configurable Detector. *Applied Physics Letters* **2006**, *89* (25), 251117.
(111) Gianoncelli, A.; Kourousias, G.; Stolfa, A.; Kaulich, B. Recent Developments at the TwinMic Beamline at ELETTRA: An 8 SDD Detector Setup for Low Energy X-Ray Fluorescence. *J. Phys.: Conf. Ser.* **2013**, *425* (18), 182001.
(112) Solé, V. A.; Papillon, E.; Cotte, M.; Walter, Ph.; Susini, J. A Multiplatform Code for the Analysis of Energy-Dispersive X-Ray Fluorescence Spectra. *Spectrochimica Acta Part B: Atomic Spectroscopy* **2007**, *62* (1), 63–68.